Physik - Department E62 - Dense and strange hadronic matter
TECHNICAL UNIVERSITY OF MUNICH

Master Thesis

Studies of the ALICE material budget between TOF and TPC with protons and pions from V^0 decays

Author
OSCAR CASTRO SERRANO

Supervisors
DR. IVAN VOROBYEV
PROF. DR. LAURA FABBIETTI

Munich, 30.09.2021

Abstract

The presence of antinuclei in cosmic rays remains one of the open questions of modern physics, with several ongoing or planned experiments looking for traces of antinuclei in space near Earth. An observation of antideuteron or antihelium nuclei in cosmic rays would most probably mean a breakthrough in searches for "new physics" such as dark matter, as the antinuclei production from ordinary collisions between cosmic rays and interstellar medium is expected to be very low, especially in the low kinetic energy range. However, to correctly interpret future results, one needs to know as precisely as possible both the antinuclei production mechanism and their nuclear inelastic cross sections. The latter defines the probability that antinuclei produced in the Galaxy can reach the detectors near Earth. Unfortunately, these inelastic cross sections are known very poorly from the experiment, which hampers precise calculations of expected antinuclei fluxes. The ALICE collaboration has recently performed novel measurements of antihelium-3 inelastic cross sections, providing the first experimental information of this kind. For these studies, precise knowledge of the detector's material budget and its description in Monte Carlo simulations is of great importance.

The Transition Radiation Detector (TRD) is one of the most dense parts at mid-rapidity of the ALICE detector at CERN LHC, dominating the material budget between the Time Projection Chamber (TPC) and the Time-Of-Flight (TOF) detectors. However, the TRD material budget which is used in ALICE Monte Carlo simulations was not validated with experimental data. At the same time, this material budget directly affects not only the studies of the (anti)nuclei inelastic cross sections, but also various ALICE analyses which employ TOF detector for particle identification.

This thesis describes a method which facilitates validation of the ALICE material between TPC and TOF detectors with protons and pions, for which the inelastic cross sections are well–known from experiment. The analysis is performed in p–Pb collisions at $\sqrt{s_{\mathrm{NN}}} = 5.02$ TeV using pure samples of protons from $\Lambda \to \mathrm{p} + \pi^-$ decays and pions from $\mathrm{K}^0_{\mathrm{S}} \to \pi^+ + \pi^-$ decays reconstructed with the Inner Tracking System (ITS) and TPC detectors. The number of protons and pions matched to a hit in the TOF detector is compared with the number of protons and pions in the TPC. The resulting TOF/TPC matching efficiency is investigated as a function of p_{TPC}, i. e. the momentum reconstructed at the TPC inner wall. Such ratio is clearly sensitive to the TRD material budget, and the experimental results are compared to those from full–scale ALICE simulations using GEANT3 and GEANT4 toolkits for propagation of particles through the ALICE detector. As a result, the material budget in question was validated with $\lesssim 5\%$ precision using protons and pions in the momentum range of $0.5 < p_{\mathrm{TPC}} < 5.0\,\mathrm{GeV}/c$.

Contents

1 Introduction

The question of the existence and the nature of the dark matter (DM) fascinates the physicists all around the world, pushing our knowledge of the physics beyond the Standard Model (SM) to the currently available experimental limits. DM is believed to be another form of matter, different from convenient visible matter, because it does interact via gravity (hence it's a "matter"), but not electromagnetically, which makes it "dark". Several hints point to the existence of a dark matter, but so far it has escaped any direct or indirect detection. The very first evidence came from Fritz Zwicky in 1933 [1], as he observed that the velocity dispersion of the different galaxies within a galaxy cluster deviates more than 400 times from the one obtained using the virial theorem considering only visible mass of the galaxies. The missing mass needed to match the observations was referred to as dark matter. Afterwards, more and more evidences of the DM existence have been found at different astronomical scales, including the observations of rotational curves of galaxies [2], the fine structure of the cosmic microwave background (CMB) [3, 4], or the gravitational lensing of galaxy clusters [5]. The DM abundance is believed to be around 27% of the total energy density budget of our universe [6]. One of the assumptions which is widely used in DM searches is that DM particles of some kind can annihilate or decay into convenient SM particles - a good candidate for such hypothetical particles are the so-called weakly interacting massive particles (WIMPs) [7].

Among other SM particles, DM annihilation or decay can also produce (anti)nuclei - composite objects made of few (anti)protons and (anti)neutrons. Recently, light antinuclei such as $\bar{\mathrm{d}}$ ($\bar{\mathrm{p}}\bar{\mathrm{n}}$), $^3\overline{\mathrm{He}}$ ($\bar{\mathrm{p}}\bar{\mathrm{p}}\bar{\mathrm{n}}$) and $^4\overline{\mathrm{He}}$ ($\bar{\mathrm{p}}\bar{\mathrm{p}}\bar{\mathrm{n}}\bar{\mathrm{n}}$) have been observed and studied at different accelerator facilities [8–16]. Currently, several models have been employed to describe the light antinuclei production [17, 18], which are mostly based on two approaches: statistical hadronization [19–21] or coalescence [22, 23]. In nature, antinuclei can be produced either from the above mentioned DM annihilations and decays or from collisions of high–energy cosmic rays (CR) with the interstellar medium. CRs are mainly high-energy protons (90%) and atomic nuclei (9% helium and 1% nuclei of higher elements) [24–27], whereas the interstellar medium is filled up mostly with hydrogen ($\approx$ 90%) and helium ($\approx$ 10%), with an average hydrogen number density of ~ 1 atom/cm^3[28].

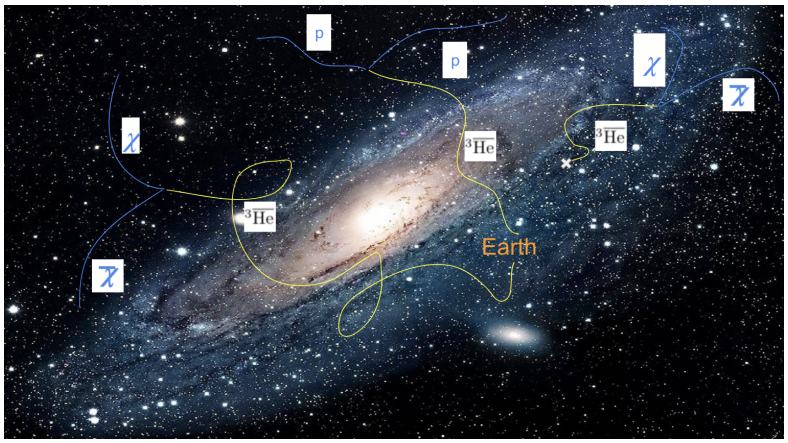

Figure 1: Graphical illustration of the $^3\overline{\mathrm{He}}$ production from cosmic–ray interactions with the interstellar gas (process in the middle) or dark–matter annihilations (process on the left). On the right–hand side another $^3\overline{\mathrm{He}}$ is produced from dark matter, but it gets absorbed before reaching us on Earth.

In fact, antideuterons and antihelium nuclei are one of the most promising probes for indirect DM searches in space, since at low kinetic energies E_{kin} the signal from DM is expected to be much higher than the background originating from cosmic–ray collisions with interstellar

medium [29–33]. Several balloon- and space-bourne experiments are currently hunting for traces of antinuclei in space, but no antideuteron or antihelium nuclei have been found so far [34–36]. In order to correctly interpret any future results, the expected fluxes of antinuclei near Earth must be calculated as precisely as possible. For this purpose one needs to know not only the aspects of antinuclei formation and propagation through the Galaxy, but also the disappearance probability of antinuclei as they can interact with the interstellar medium on the way to our detectors. This probability is defined by the nuclear inelastic cross section, which unfortunately remains poorly known for antideuteron and antihelium.

Recently, the ALICE collaboration has studied the antideuteron inelastic cross section using the detector material as an effective target [37]. The Large Hadron Collider at CERN provides a perfect environment to study the physics of (anti)nuclei, since the collision energies available there allow to produce matter and anti-matter in large and equal abundances [19, 38]. Excellent tracking and Particle IDentification (PID) capabilities of ALICE make it possible to study the (anti)nuclei production and annihilation down to very low momentum. Recently, these novel studies have been extended to $^3\overline{\mathrm{He}}$ nuclei, for which $^3\overline{\mathrm{He}}$ have been identified with the help of the Time Projection Chamber (TPC) and the Time-of-Flight (TOF) detectors [39]. $^3\overline{\mathrm{He}}$ nuclei reconstructed in the TPC have been matched to a hit in TOF, making it possible to extract the inelastic cross section of $^3\overline{\mathrm{He}}$ on an effective target material between TPC and TOF. However, for these studies it is crucial to know the ALICE material budget between TPC and TOF used in the Monte Carlo simulations, which is mainly represented by the Transition Radiation Detector (TRD) [40].

Figure 2 shows cumulative material budget of the ALICE apparatus at mid-rapidity as a function of radius from the nominal collision point as used in the Monte Carlo simulations [37] (more detailed description of the ALICE apparatus is presented in Chapter 2). The results are shown in units of radiation length X_0, which is a material–specific constant defined as 7/9 of the mean free path for pair production of a high-energy photon. It can be seen that the material budget stays low up to the outer TPC wall, but significantly increases beyond this point. The TRD material, with a total X_0 of $\sim 24.7\%$ [40], plays here a central role.

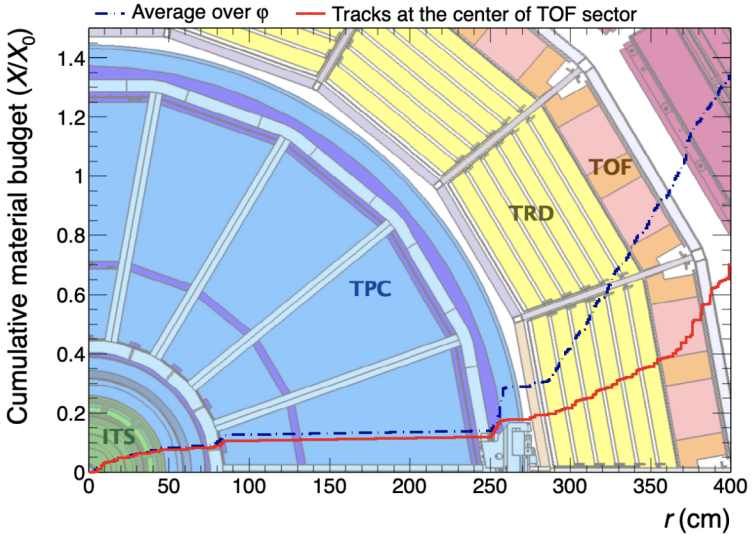

Figure 2: Cumulative material budget of ALICE detectors as a function of the radial distance to the collision point, in units of X_0. The red line corresponds to the straight primary tracks emitted perpendicularly to the beam line at the center of the TOF sectors, whereas the blue one represents mean material budget averaged over azimuthal angle.

In order to precisely describe the detector performance and response, the ALICE material

budget should be known as precise as possible. For this purpose, the pair production $\gamma \longrightarrow e^+ + e^-$ processes taking place in the detector material can be used, which happen with a well-known probability and can be reconstructed using their characteristic V^0 topology (referring to the V-shape of two daughter particles originating from neutral mother decay). By comparing the results from experimental data and from Monte Carlo simulations, the ALICE material budget up to the middle of the TPC (i.e. up to radius of ~ 170 cm) could be validated with this method within 4.5% [41] as shown in Fig. 3.

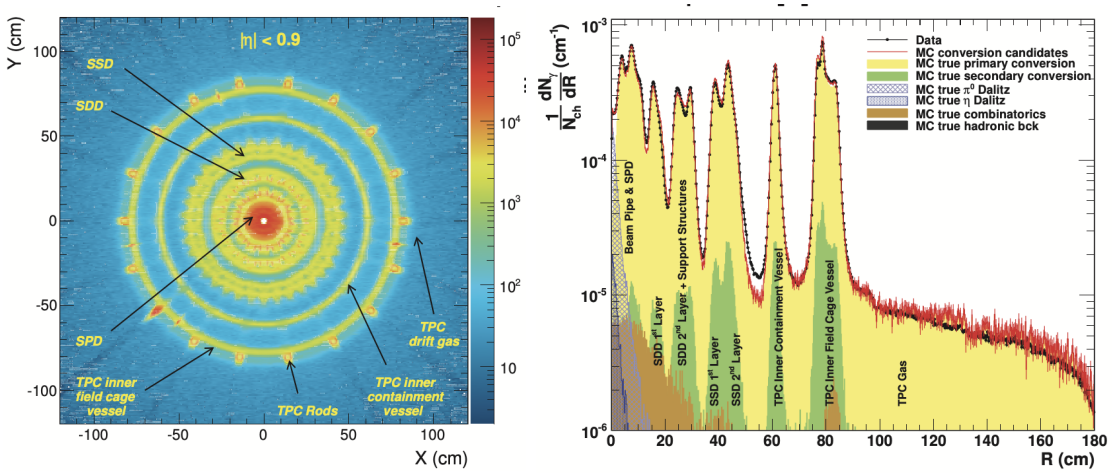

Figure 3: The xy positions of reconstructed vertices of photon conversions in the ALICE detector material (left) and the comparison between data and MC as a function of radius (right) from [41]

However, this method is clearly not applicable for the detector material beyond that point, since no detector can reconstruct the γ conversions. Furthermore, the detector material located between TPC and TOF affects not only the aforementioned studies of antinuclei inelastic cross sections in ALICE, but essentially all analyses utilising the information from various detectors such as High-Momentum Particle Identification Detector (HMPID), ElectroMagnetic CALorimeter(EMCAL) and TOF itself. The description of this material budget used in Monte Carlo simulations was not yet validated with experimental data.

This thesis presents a method which allows one to study the material budget between TPC and TOF using protons and pions, for which the inelastic cross section of interactions with the detector material is well–known from experiment. Pure samples of these hadrons are obtained using the V^0 decays of $\Lambda \longrightarrow p + \pi^-$ for protons and $K^0_S \longrightarrow \pi^+ + \pi^-$ for pions. Their charged–particle tracks are reconstructed in the TPC and propagated to the TOF detector, where they can be matched to a TOF hit if hadron didn't undergo inelastic interaction in the detector material beforehand. A schematic idea of this analysis can be seen in fig. 4. This TOF-to-TPC matching efficiency is analysed as a function of the momentum and is compared to the results from MC simulations using GEANT3 and GEANT4 toolkits for the propagation of particles through the ALICE detector. This ratio is clearly affected by the detector acceptance and by inelastic interactions of pions and protons in the detector material, but these aspects can be well described by MC simulations. Moreover, the TOF/TPC matching efficiency is sensitive to the difference in the material budget in data and simulations. The material budget can therefore be constrained via the comparison of experimental results with MC simulations.

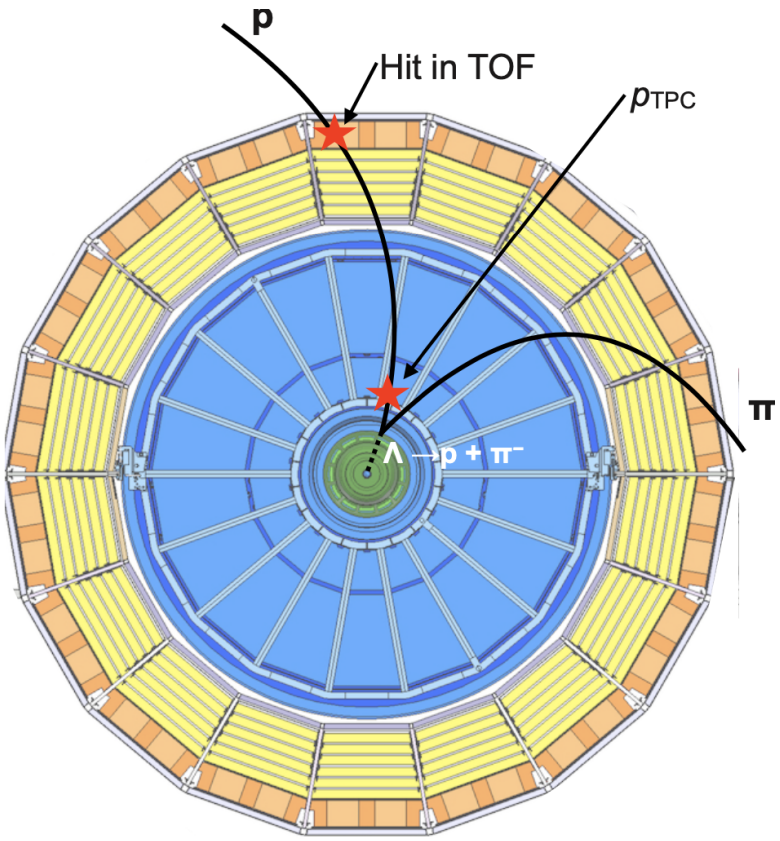

Figure 4: Schematic view of the Λ decay showing the idea of the analysis (analogously for $K^0_S \longrightarrow \pi^+ + \pi^-$ decay). A proton track originating from the Λ decay is reconstructed in the TPC and reaches the TOF detector, where its hit is matched to the TPC track.

The thesis is structured in the following way. Chapter 2 describes the ALICE apparatus and its different sub-detectors. The details about the data analysis including Monte Carlo simulations are presented in Chapter 3. Chapter 4 describes systematic checks and uncertainties performed in the analysis. The results are discussed in Chapter 5, and the thesis is concluded with summary and outlook in Chapter 6.

2 The ALICE Experiment

ALICE stands for A Large Ion Collider Experiment and, as its name suggests, focuses on studies of heavy–ion collisions and the physics of strongly interacting matter at the highest energy densities reached so far in the laboratory. A complete description of the detector's composition and its performance can be found in [41, 42]. The data collected during proton–proton and proton–ion LHC runs serve both as baseline for comparisons with nucleus-nucleus collisions and are analysed in their own right. The purpose of the detector and the need to cope with large number of charged–particle tracks created in collisions drives the detector's design which is shown in Fig. 5. The sub-detectors located at mid-rapidity are surrounded by large solenoid magnet (shown in Fig. 5 in red) which provides uniform magnetic field of 0.5 T along the beam axis. The sub-detectors relevant for this analysis are described in more details below.

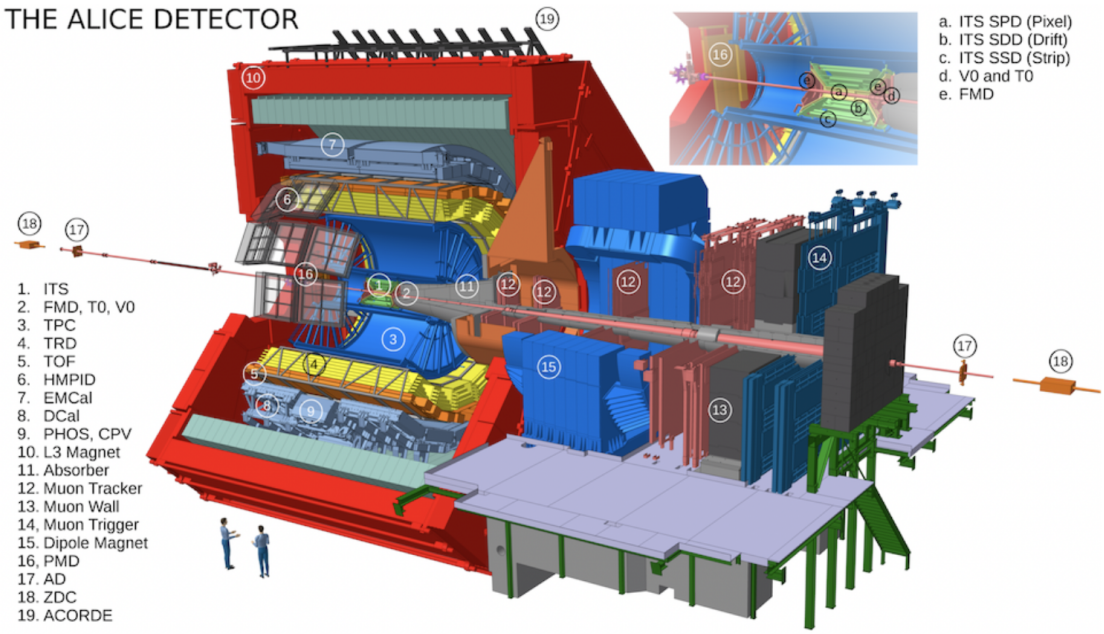

Figure 5: Overview of ALICE detectors during Run 2 (2015-2018)

2.1 Inner Tracking System (ITS)

The ITS is the closest detector to the beam pipe, where the collisions take place. In Fig. 5 it is highlighted in green. A more detailed view of the ITS can be seen in figure 6.

The ITS is constituted by six cylindrical layers of silicon detectors, which are located at the following radial distances: 4, 7, 15, 24, 39 and 44 cm. There are, in turn, three types of detectors (going from the collision point outwards): two Silicon Pixel Detectors (SPD), two Silicon Drift Detectors(SDD), and two Silicon Strip Detectors(SSD).

The ITS can fulfill the following tasks:

- Setting the location of the primary collision vertex and secondary vertices from hadronic decays with a resolution better than 100 μm
- Improvement of the impact parameter and momentum resolution of charged particle tracks reconstructed in the TPC

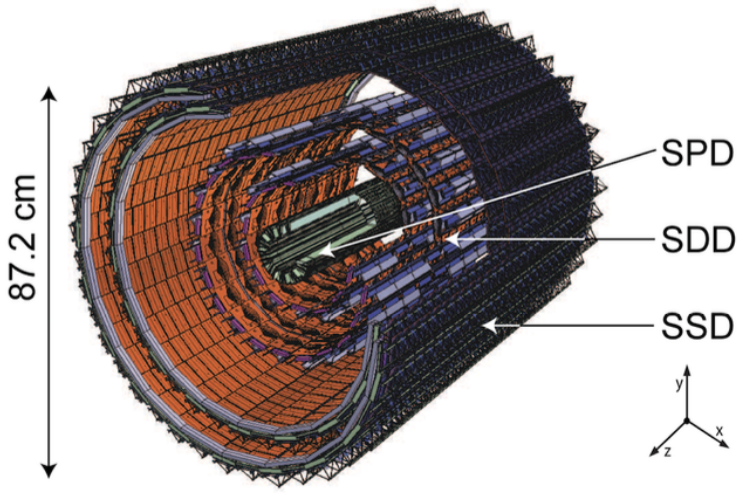

Figure 6: View of the ITS and its subdetectors [43]

- Tracking and identification of particles with $p_T < 200 MeV/c$ which are not detected in the TPC, thanks to the information on the energy loss in SDD and SSD layers [42]

Since the momentum and impact parameter resolution for low-momentum particles are dominated by multiple scattering effects in the detector material, the amount of material has been kept to a minimum, which is another key feature of the ITS detector. Fig. 7 shows how this quantity increases with the different layers of ITS. The total X_0 assigned to ITS sums up to 8%, which is dominated by silicon active detector areas and carbon supporting structures.

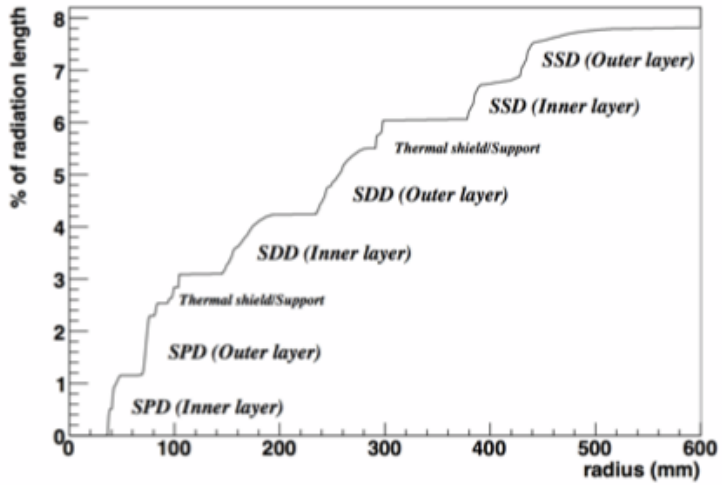

Figure 7: ITS material thickness versus radius

2.2 Time Projection Chamber (TPC)

The TPC is the main charged-particle tracking device in the ALICE central barrel. It is 5m long and has a radius extending from 85 cm to 247 cm, which makes it the largest TPC detector in

the world. In Fig. 5, the TPC is sketched in blue, around the ITS. In Fig. 8 we can see the schematics of the TPC. A detailed description of the TPC can be found in [44].

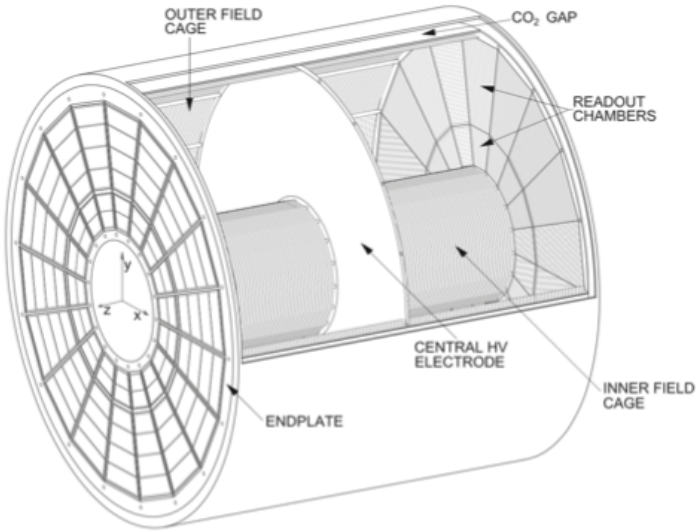

Figure 8: Schematic representation of the TPC detector [43]

The TPC is a gas detector covering the whole azimuthal angle, with a pseudorapidity acceptance of $|\eta| \leq 0.9$ for full radial track length. For the time where the data for this analysis were taken (2016), the TPC was filled with a gas mixture of $Ar - CO_2$ with fraction 88/12 (also in 2018). In 2017 the mixture was $Ne - CO_2 - N_2$, with fraction 90/10/5. The TPC inner and outer walls are made of composite structures with a Nomex honeycomb core sandwiched between prepreg sheets (epoxy fiberglass) and Tedlar foils. The total radiation length of TPC amounts to $X_0 = 3.5\%$ near mid-rapidity.

Charged particles produced in collisions traverse the gaseous volume of the TPC and cause an ionisation of gas atoms, producing electrons and ions. Primary ionized electron-ion pairs are separated by a high electric potential difference between the endplates and the central cathode, with electric field parallel to the beam pipe. Due to this electric field, positively charged ions drift towards the cathode and are neutralized, whereas the electrons are forced towards the readout chambers located at the endplates of the TPC, where they are read out in Multi Wire Proportional Chambers (MWPCs). The endplates are segmented into 18 modules in azimuthal direction, as can be seen in Fig. 8. 159 pad rows in radial direction provide track points in the xy plane. The third dimension is given by the time the electrons need to make it to these endplates with constant drift velocity, granting us with a full 3-dimensional description of a charged-particle track. Tracks reconstructed in the TPC can be matched to ITS hits or to the outer detectors such as TRD and TOF.

The Particle IDentification (PID) is based on the energy loss in the TPC gas, which can be described by the Bethe-Bloch formula:

$$-\left\langle \frac{dE}{dx} \right\rangle = \frac{4\pi n}{m_e c^2 \beta^2} \cdot \left(\frac{ze^2}{4\pi\epsilon_0} \right)^2 \left[\ln\left(\frac{2m_e c^2 \beta^2}{I \cdot (1-\beta^2)} \right) - \beta^2 \right]. \tag{1}$$

Here $\beta = v/c$ is the fraction of the velocity v of the particle and speed of light c, ϵ_0 is the electric field constant, e is the elementary charge, z is the charge of the particle, n is the electron density of the material, m_e is the mass of the electron and I is the average excitation potential

of the material. Using the curvature of the charged-particle tracks introduced by the presence of magnetic field and of the consequent Lorentz force, one can calculate the momentum p of the traversing particle. Taking the following relativistic relationship,

$$p = m_0 \beta \gamma \tag{2}$$

we can eliminate the β dependence in Equation 1 in favour of the m_0 dependence, thus having a relationship between the energy loss and the mass of the particle. Therefore, simultaneous measurement of particle's momentum and energy loss gives an information on the particle's mass. In Fig. 9 the energy loss distribution in the TPC as a function of the particle momentum p is shown. One can see that different particle species (pions, electrons, kaons, protons and deuterons) can be identified and separated over the large momentum range. However, one can see that the bands of the different particles overlap at some point (for instance, the protons band overlaps with electrons band at around 1 GeV/c , and merges with pions and kaons at around 1.8 GeV/c). In order to be able to distinguish these particles at higher momenta, one needs to use complementary signal from other detectors like the Time-Of-Flight, which is described below.

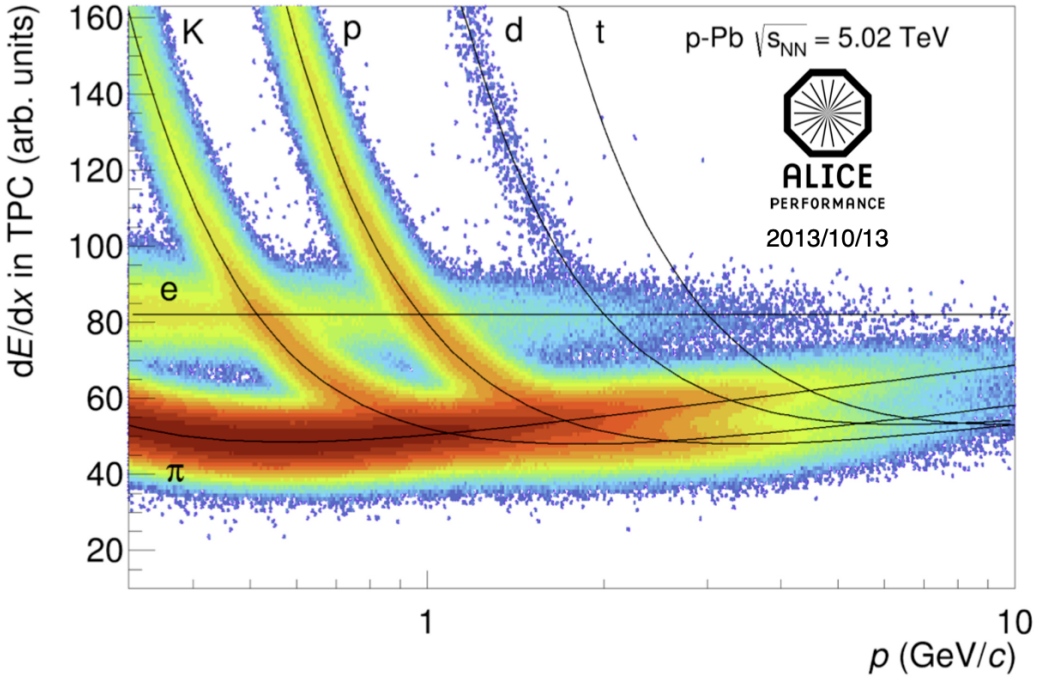

Figure 9: dE/dx as a function of momentum p measured in ALICE p–Pb collisions. The black lines are the theory predictions given by the Bethe-Bloch formula.

2.3 Transition Radiation Detector (TRD)

The main goal of the TRD is to discriminate electrons and positrons from other charged particles (mostly pions) using the transition radiation, X-rays emitted when the particles cross many layers of thin materials. Referring again to Fig. 5, the TRD is shown in yellow surrounding the TPC. In order to follow the partition of the latter, the TRD also consists of 18 supermodules as can be seen in Fig. 10. Each supermodule is composed of six layers of five drift chambers, filled

with a mixture of Xe and CO_2, with a proportion of 85/15. The TRD is installed inside the stainless-steel space frame which surrounds the TPC.

The material budget of the TRD plays central role in this analysis. As already mentioned in the previous section, the TRD is the detector with the highest radiation lenght at mid-rapidity, with a total $X_0 = 24.7\%$. Detailed composition of each single TRD readout chamber can be found in Table 1.

Table 1: List of materials of a single TRD readout chamber [40]

Material	Description	Thickness [cm]	Density [g/cm^3]	X/X$_0$ [%]
Mylar	Mylar layer on radiator	0.0015	1.39	0.005
Carbon	Carbon fiber mats	0.0055	1.75	0.023
Araldite	Glue on the fiber mats	0.0065	1.12	0.018
Rohacell	Sandwich structure	0.8	0.075	0.149
PP	Fiber mats inside radiator	3.186	0.068	0.490
Xe/CO_2	The drift region	3.0	0.00495	0.167
Xe/CO_2	The amplification region	0.7	0.00495	0.039
Copper	Wire planes	0.00011	8.96	0.008
Copper	Copper of pad plane	0.0025	8.96	0.174
G10	PCB of pad plane	0.0356	2.0	0.239
Araldite	Glue on pad plane	0.0923	1.12	0.107
Araldite	+ additional glue (leaks)	0.0505	1.12	0.107
Carbon	Carbon fiber mats	0.019	1.75	0.078
Aramide	Honeycomb structure	2.0299	0.032	0.169
G10	PCB of readout boards	0.0486	2.0	0.326
Copper	Copper of readout boards	0.0057	8.96	0.404
Copper	Electronics and cables	0.0029	8.96	0.202

2.4 Time-of-Flight (TOF)

At mid-rapidity, the PID performance of ITS and TPC is complemented by the TOF detector. As its name states, this detector measures the time of flight of a particle between the collision point and the detector itself. In Fig. 5, the TOF detector is highlighted in orange, surrounding the TRD. A schematic layout of the detector can be seen in Fig. 11.

The TOF covers a radial distance to the collision point between 3.70m (inner radius) and 3.99m (outer radius), and is divided as well in 18 supermodules, which contain around 160000 readout pads. The starting time of the flight (i.e. the collision time) is provided by T0 detectors comprising two Cherenkov counters located at forward rapidity. The TOF detector reaches a time resolution lower than 100 ps to determine the time a particle spends until it hits the detector. Tracks reconstructed in the ITS and TPC are matched to TOF hits, thus providing us with the information about the particle's momentum (from ITS and TPC) and $\beta = v/c$ (from the time of flight). According to Eq. 2 this combined measurement gives us information about the mass of the particle as can be seen in Fig. 12. In this figure several bands can be observed for the different particle species, which are separated from each other over wide momentum range.

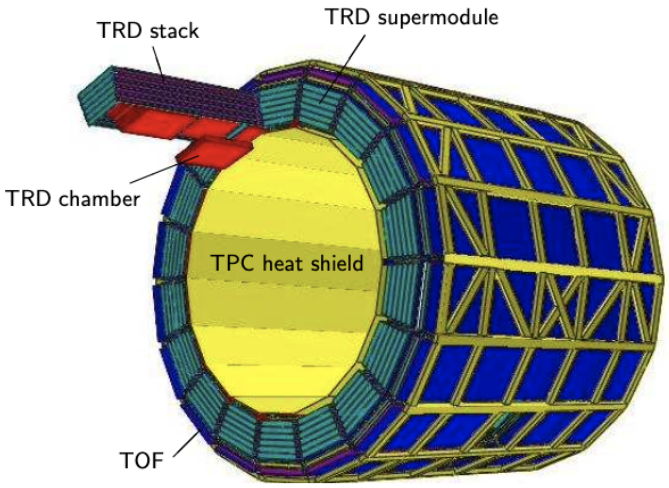

Figure 10: The TRD detector installed on space frame, with one of the 18 supermodules highlighted in red.

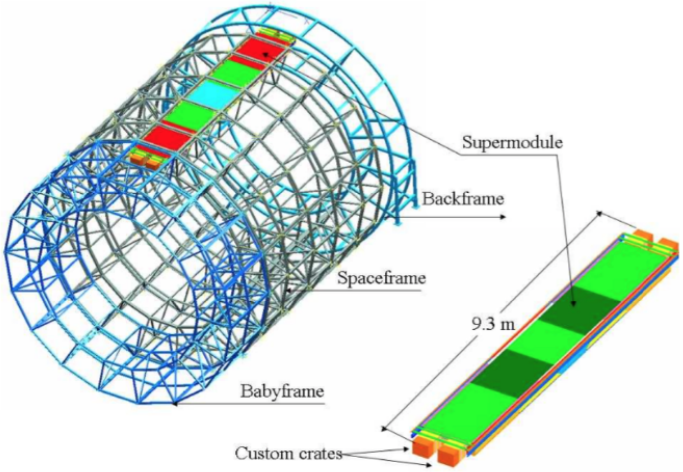

Figure 11: Layout of TOF detector [42] and of one of its supermodules

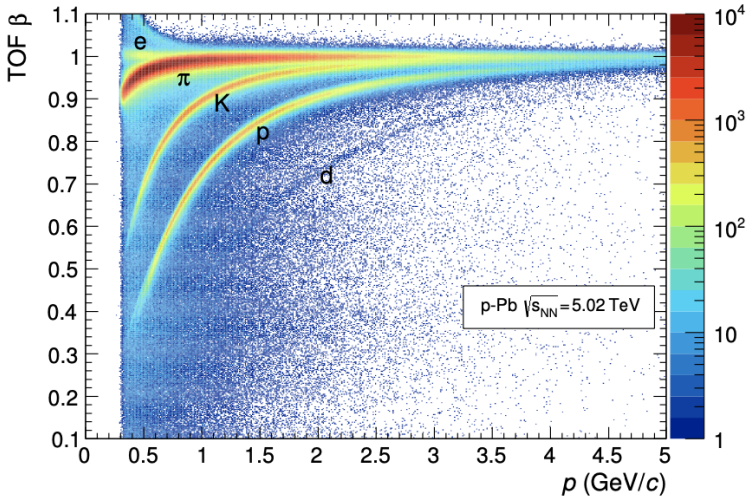

Figure 12: TOF β as a function of momentum p as measured by the TOF detector in p–Pb collisions [41]

3 Data Analysis

3.1 Datasets and Event Selection

The experimental data for this analysis have been collected during 2016 p–Pb LHC run at the collision energy of $\sqrt{s_{\mathrm{NN}}} = 5.02\,\mathrm{TeV}$. Collision events are selected using so-called minimum–bias (MB) trigger requirement, which is provided by the V0 detector comprising two scintillator arrays in the pseudorapidity ranges of $2.8 < \eta < 5.1$ and $-3.7 < \eta < -1.7$. The MB trigger signal consists of simultaneous signals in two scintillator arrays. In addition to the trigger requirement, background events (like collisions of de-bunched protons and ions and collisions with mechanical structures of the beam line or with gas) are rejected using the information from two innermost layers of the ITS detector and from the V0 detector. For primary collision vertex the following requirements are applied:

- Vertex position within $\pm 10\,\mathrm{cm}$ from the geometrical centre of the detector along beam axis
- At least 1 track/tracklet contributing to the vertex reconstruction
- Rejection of SPD vertices for which only z coordinate is reconstructed and it is determined with poor resolution
- Cut on absolute distance between vertices reconstructed with tracks and with SPD tracklets (with max. displacement $= 0.5\,\mathrm{cm}$)

To make sure that all detectors used in track reconstruction cover the central pseudorapidity region of $|\eta| < 0.8$ with uniform acceptance, vertex position is required to be within $\pm 10\,\mathrm{cm}$ from the geometrical centre of the detector along the beam axis (Fig. 13), with $\sim 13\%$ of all events lying outside of these limits. In total $N_{\mathrm{MB}} = 286.8 \times 10^6$ minimum bias events are selected for further analysis on single track level.

In this analysis Monte Carlo simulated data are used to compare the absorption of protons and pions in the detector material between TPC and TOF with the experimental data. The two Monte Carlo samples used in the analysis employ DMPJET event generator [45] and GEANT toolkit for propagation of (anti)particles through the detector material. The only difference between two samples is the GEANT version (GEANT3 and GEANT4) [46, 47], which gives an opportunity to directly compare two versions. With the Monte Carlo data, the analyses of both primary and secondary (from V^0 decays) protons and pions are possible, since in Monte Carlo pure hadrons can be selected using their PDG codes.

3.2 V^0 and Track Selection

Figure 14 sketches a decay of a neutral particle into two charged daughter particles, where M is the original (mother) particle and m_1, m_2 the produced (daughter) particles, in the center-of-mass (CM) frame. Such process is typically referred to as a V^0 decay, and there are three different types of such decays typically present in the experimental data: $\mathrm{K}^0_{\mathrm{S}} \longrightarrow \pi^+ + \pi^-, \Lambda \longrightarrow p + \pi^-$ and the conversion of real photon in the detector material $\gamma \longrightarrow e^+ + e^-$.

To be able to distinguish among them, one can make use of the Armenteros Podolanski variables, which correspond to the variables plotted on the axis of Fig. 15. Those variables are the transverse momentum q_t (the momentum component of one of the daughter tracks perpendicular to the parent momentum vector) and the variable α which is related to the asymmetry in the longitudinal momentum of the daughter particles:

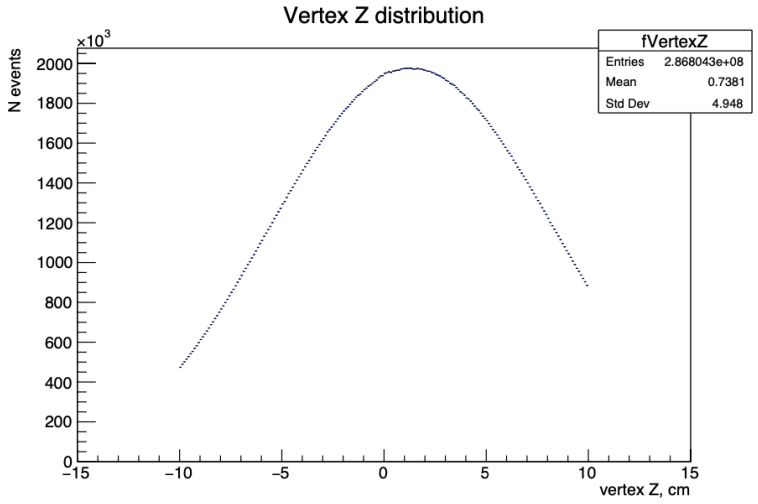

Figure 13: Distribution of vertex Z position in events selected for the analysis.

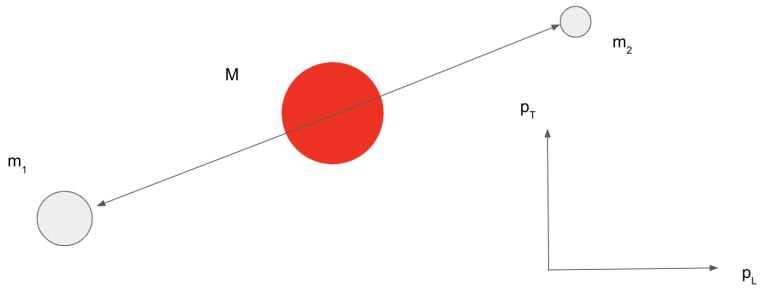

Figure 14: Sketch of the Decay in the CM frame

$$\alpha = \frac{p_L^{(1)} - p_L^{(2)}}{p_L^{(1)} + p_L^{(2)}} \tag{3}$$

The detailed mathematical derivation of these variables can be seen in the Appendix. In this plot one can find a clear separation among the three decays, with the decays of Λ and K^0_S being represented by an ellipsoidal band (see more details in Appendix). One can see some characteristic properties of these decays, e.g. K^0_S and γ decays are symmetric, since the α values are centered at 0. However, they are well separated from each other by the q_t value, as photon has no intrinsic mass to give its daughter particles any transverse momentum. Regarding the Λ decay, this has a similar argument as for the K^0_S in terms of q_t, but this decay is clearly asymmetric, since most of the momentum of mother particle is carried away by heavy proton (and so $\alpha = [0.4, 1]$).

In order to select well-reconstructed decays of Λ and K^0_S originating from primary event vertex and to suppress contribution from photon conversions in the detector material, several V^0 selection criteria are applied as listed in Table 2. The V^0 decay radius represents here the radial distance between the primary collision vertex and the secondary vertex of the V^0 decay. The pointing angle ϕ refers to the angle between the reconstructed momentum vector of the V^0 candidate and the straight line connecting secondary and primary vertices. DCA^{V0}_{xy} is the distance of closest approach between the mother particle and the primary vertex in a plane

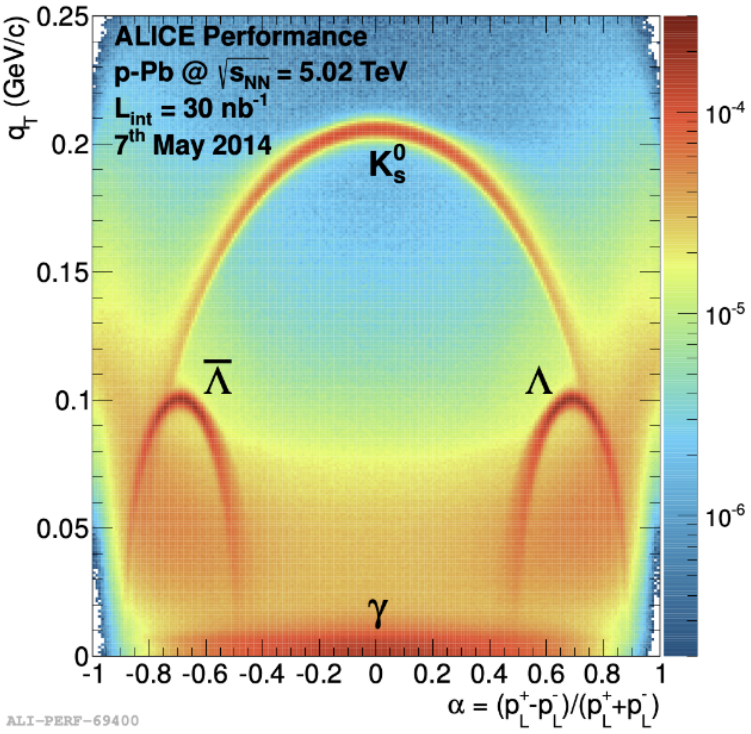

Figure 15: Armenteros-Podolanski plot in p–Pb collisions in ALICE.

perpendicular to the beam direction.

Λ and K^0_S candidates are accepted for the analysis if the invariant mass of daughter track pair is within the limits listed in Table 2. The limits correspond to about $\pm 1\sigma$ range around the nominal mass, where 1σ is the detector's mass resolution. The selection on the Armenteros–Podolanski q_t further improves the discrimination between the two types of decay in question. It also suppresses photon conversion in the detector material. Candidates which, under the corresponding mass assumptions for daughter tracks, have an invariant mass consistent with both $\Lambda \to \mathrm{p} + \pi^-$ and $\mathrm{K}^0_\mathrm{S} \to \pi^+ + \pi^-$ decays are rejected from the analysis.

Table 2: V^0 selection criteria used in analysis

Variable	Requirement
Pseudorapidity	$\lvert\eta\rvert < 0.5$
Transverse momentum	$p_\mathrm{t} > 0.3\,\mathrm{GeV}/c$
V^0 decay radius	$0.2 < r_{xy} < 40$ cm
Pointing angle	$\cos\phi > 0.99$
DCA of V0 to prim. vertex	$\mathrm{DCA}^{V0}_{xy} < 0.2$ cm
Λ mass selection/rejection	$1.112 < m_{\mathrm{p}\pi} < 1.120$ GeV/c^2
Λ q_t selection/rejection	$0.02 < q_t < 0.11\,\mathrm{GeV}/c$
K^0_S mass selection/rejection	$0.48 < m_{\pi\pi} < 0.515$ GeV/c^2
K^0_S q_t selection/rejection	$q_t > 0.11\,\mathrm{GeV}/c$

Figures 16, 17 and 18 show the corresponding distributions for selected Λ candidates, and Figs. 19, 20 and 21 for K^0_S candidates.

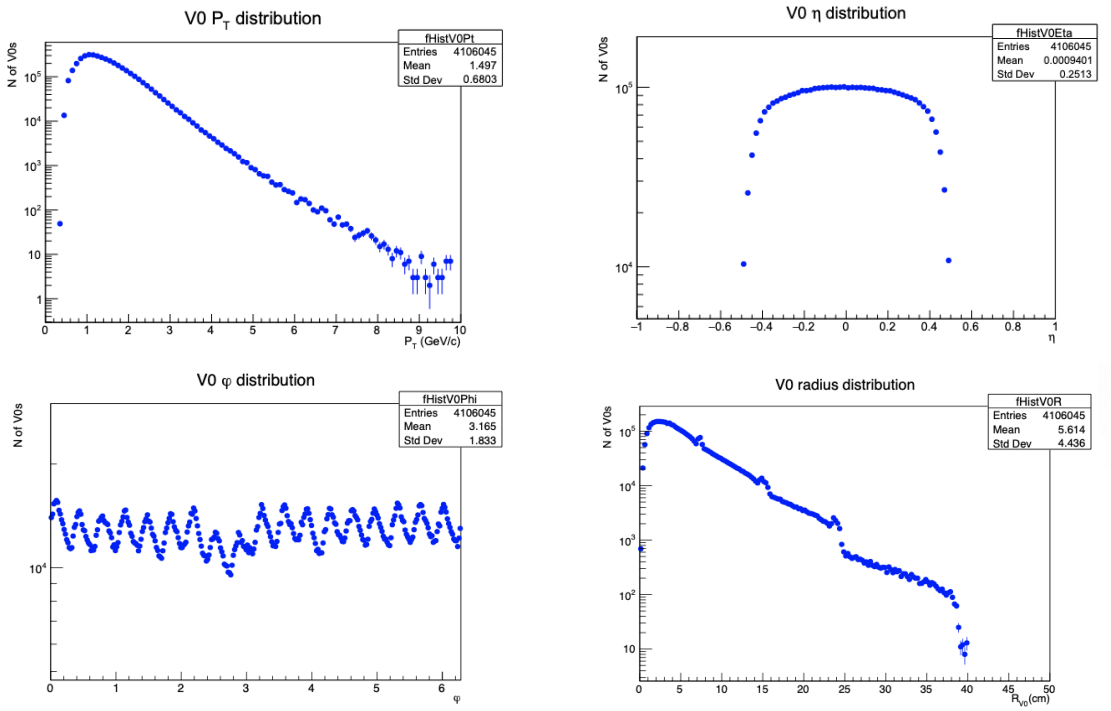

Figure 16: p_t, η, φ and decay radius distributions of selected Λ candidates.

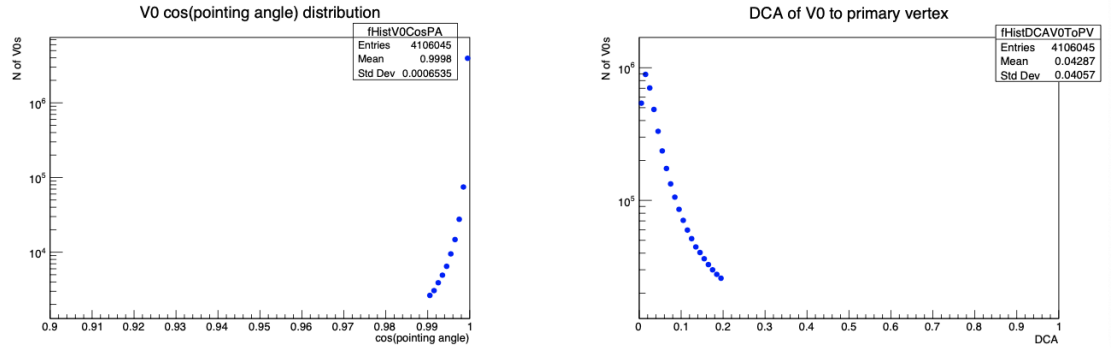

Figure 17: Cosine of pointing angle and DCA to primary vertex of selected Λ candidates.

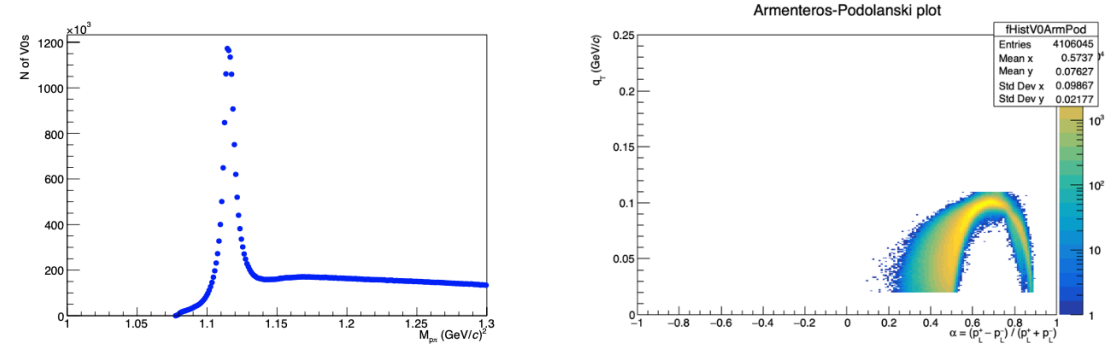

Figure 18: Invariant mass distribution (before the cut on Λ mass) and Armenteros-Podolanski plot for selected Λ candidates.

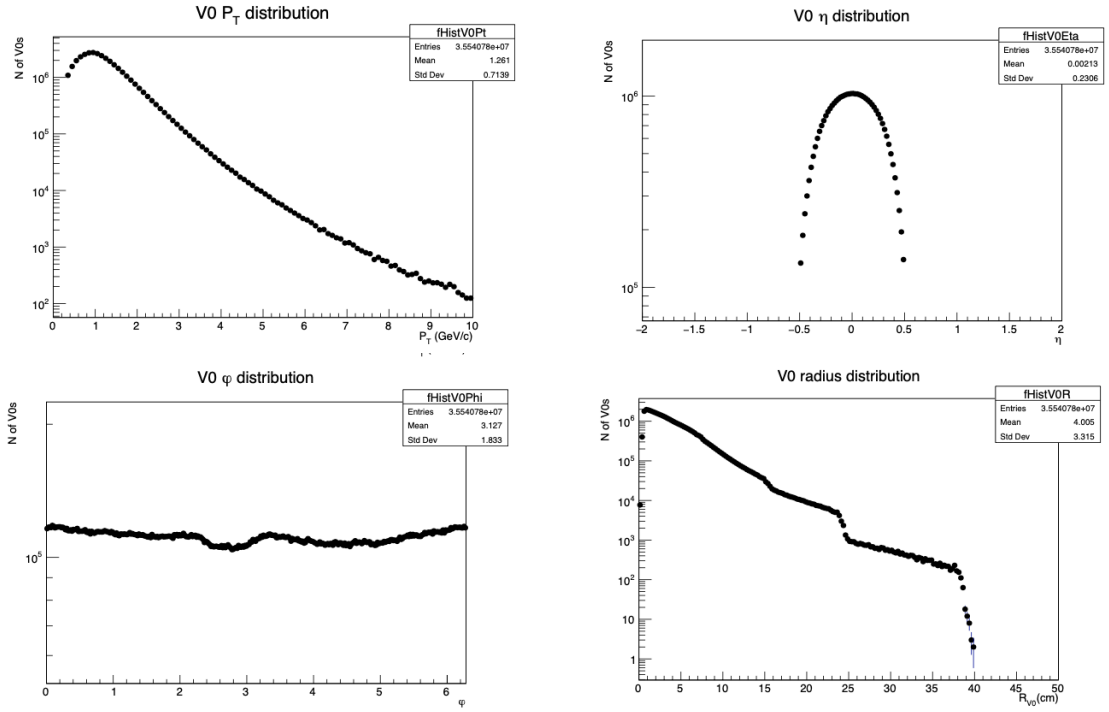

Figure 19: p_t, η, φ and decay radius distributions of selected K^0_S candidates.

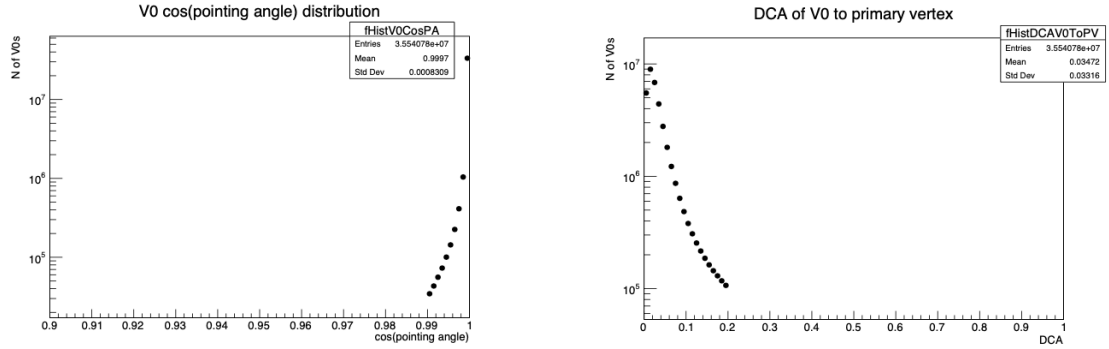

Figure 20: Cosine of pointing angle and DCA to primary vertex of selected K^0_S candidates.

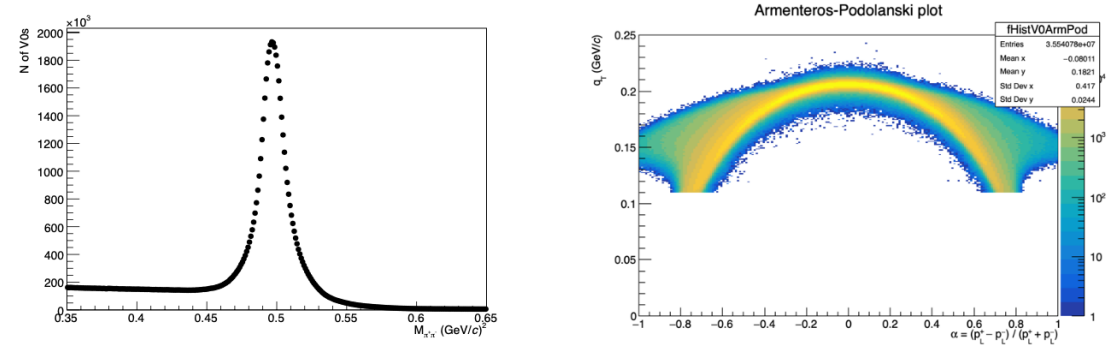

Figure 21: Invariant mass distribution (before the cut on K^0_S mass) and Armenteros-Podolanski plot for selected K^0_S candidates.

3.3 Daughter Track Selection

On top of the selection described in previous subsection, tracks originating from V^0 decays are required to pass the selection criteria which are summarised in the Table 3. The number of TPC clusters represents the amount of clusters associated to the track from daughter particle (out of maximum 159); the same stands for the ITS clusters (out of maximum 6). The DCA to primary vertex is the distance of the closest approach between track and primary vertex in perpendicular plane to the beam direction. It was chosen to be larger than 0.05 cm in order to suppress contribution from primary hadrons originating from the event collision vertex. The PID selection is based on the TPC PID signal and uses the number of standard deviations (sigmas) between the theoretical value of the energy loss in the TPC gas for given particle hypothesis and the experimentally observed value:

$$n(\sigma_h^{TPC}) = \frac{(dE/dx)_{measured} - \langle dE/dx \rangle(h)}{\sigma_h} \tag{4}$$

Figures 22 and 23 show the corresponding distributions for proton candidates from Λ decays, and Figures 24 and 25 for pions from K^0_S decays.

Table 3: Daughter track cuts used in analysis

Variable	Requirement
Pseudorapidity	$\|\eta\| < 0.5$
N of TPC clusters	≥ 80
N of ITS clusters	≥ 2
DCA to prim. vertex	$\mathrm{DCA}_{xy} > 0.05$ cm
PID selection	$\|\mathrm{TPCn}\sigma\| < 3$

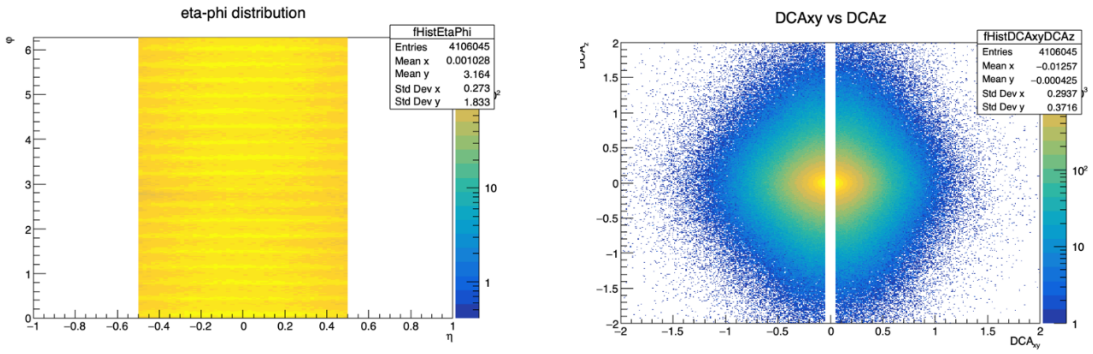

Figure 22: $\eta\varphi$ and DCA distributions of selected proton candidates from Λ decays.

The V^0 and track selection described above provides high-purity samples of protons (from Λ decays) and pions (from K^0_s decays) in the TPC, and the only PID selection applied for the proton and pion candidates is the requirement of corresponding $|\mathrm{TPCn}\sigma|$ to be less than 3. In the TOF detector selected tracks are required to have matched TOF hit, but no further selection (on TOF signal or TOF mass) is applied. Figures 26 and 27 show the TPC and TOF PID signal for selected proton and pion candidates.

As it can be seen from Figures 26 and 27, the resulting purity of selected protons and pions is indeed very high, with only some contamination visible in the TOF β histograms in the momentum range of about $1.2 < p < 3\,\mathrm{GeV}/c$ (in TPC these particles cannot be distinguished from each other in this momentum range). In order to investigate the contamination from pions

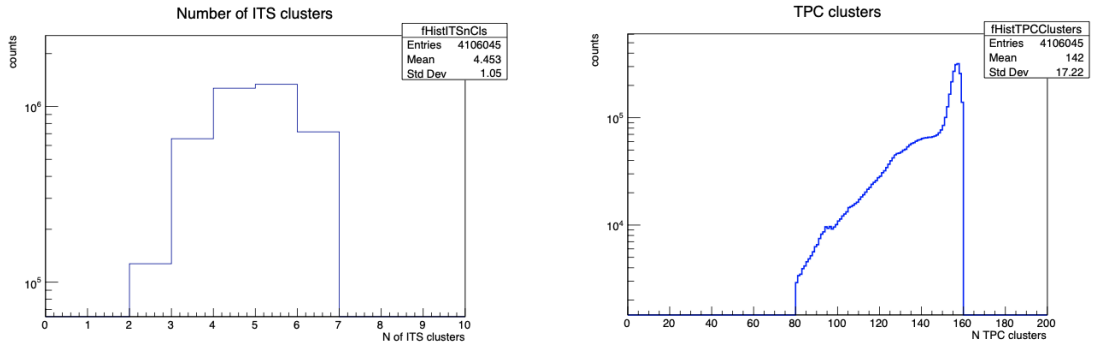

Figure 23: Number of ITS and TPC clusters for selected proton candidates from Λ decays.

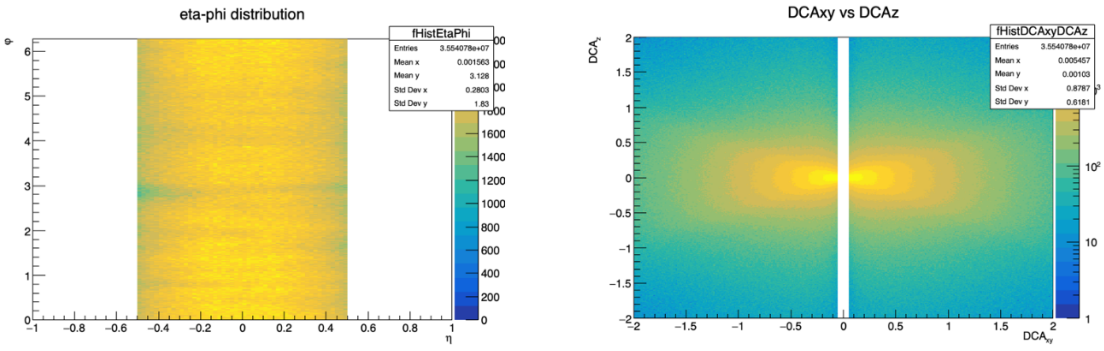

Figure 24: $\eta\varphi$ and DCA distributions of selected pion candidates from K^0_S decays.

in proton sample in more details, the $TOF_{n\sigma\pi}$ distributions are analysed for selected protons in each momentum bin, and the pion peak is fitted with the gaussian function as shown in Fig. 28. The contamination from pions is then estimated bin−by−bin as the ratio of pion peak integral to all particles in that momentum bin. The same strategy is also applied for the estimation of proton contamination in pion sample, for which $TOF_{n\sigma prot}$ distributions are analysed bin−by−bin for selected pions (Fig. 29).

The resulting purity of proton and pion samples is found to be $> 97.5\%$ in all momentum bins as shown in Fig. 30. Since in the momentum range with non-zero contamination it's not possible to distinguish protons and pions in the TPC, both contamination from pions in proton sample and the one from protons in pion sample are not rejected in the final results. This means that TOF/TPC ratios are shown for all particles selected as described above (including contamination), and the corresponding effect on the final results is described in Section 4.

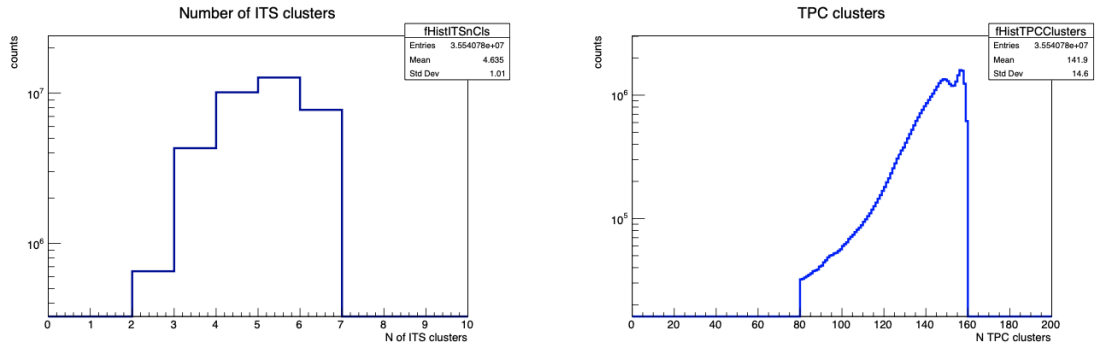

Figure 25: Number of ITS and TPC clusters for selected pion candidates from K^0_S decays.

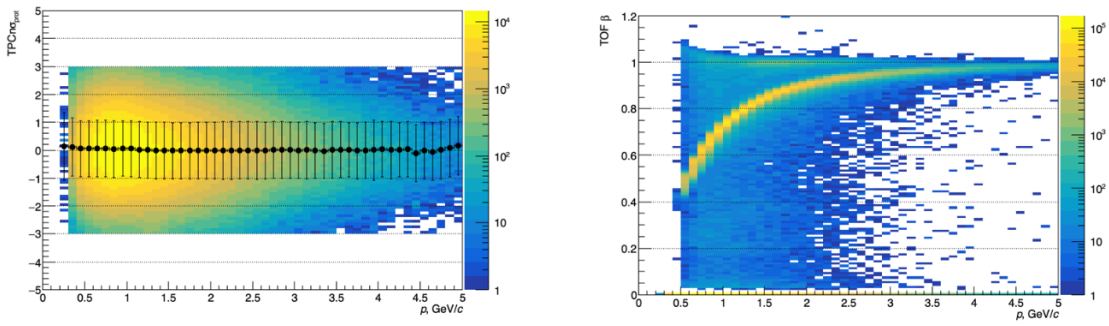

Figure 26: TPC$n\sigma$(proton) and TOF β as a function of momentum p for selected proton candidates. Black points on the left plot show the 1D profile of the histogram, with uncertainties corresponding to 1 RMS of TPC$n\sigma$(proton) distribution in each momentum bin.

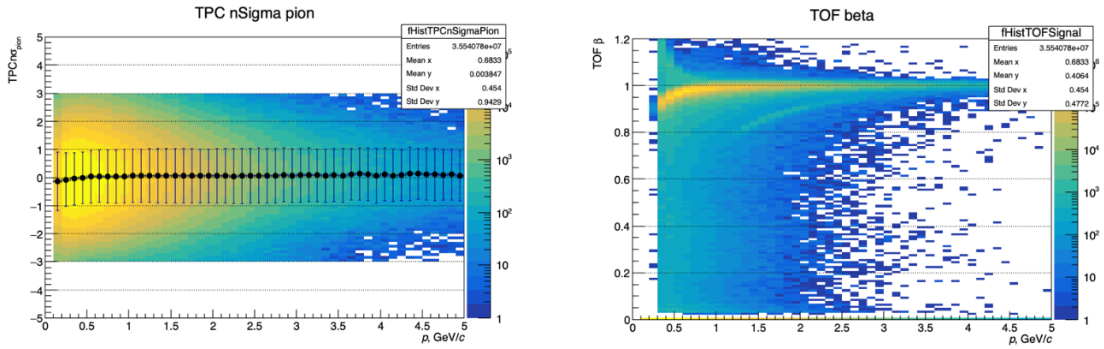

Figure 27: TPC$n\sigma$(*pion*) and TOF β as a function of momentum p for selected pion candidates. Black points on the left plot show the 1D profile of the histogram, with uncertainties corresponding to 1 RMS of TPC$n\sigma$(pion) distribution in each momentum bin.

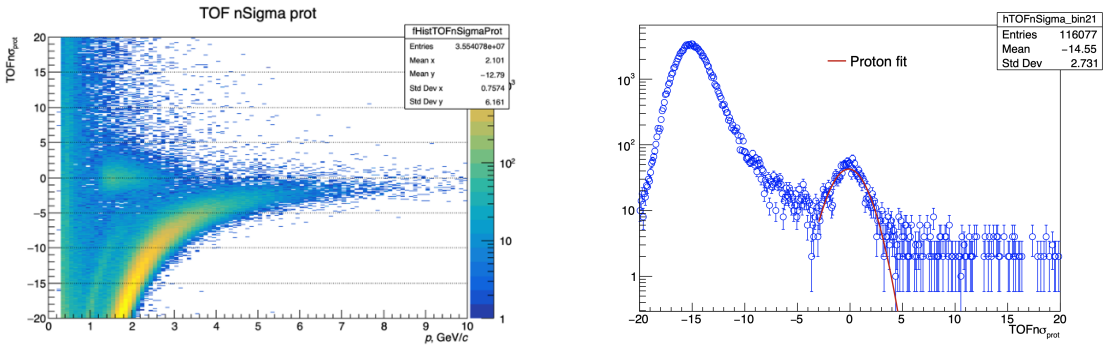

Figure 28: Left: TOF$n\sigma$(proton) as a function of momentum for selected proton candidates. Right: gaussian fit (red line) to the proton peak in the momentum bin $2.0 < p < 2.1\,\mathrm{GeV}/c$.

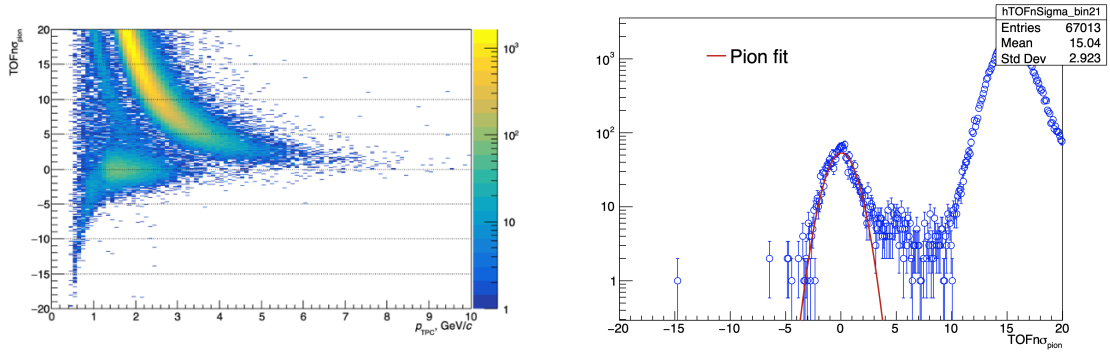

Figure 29: Left: TOF$n\sigma$(pion) as a function of momentum for selected pion candidates. Right: gaussian fit (red line) to the pion peak in the momentum bin $2.0 < p < 2.1\,\mathrm{GeV}/c$.

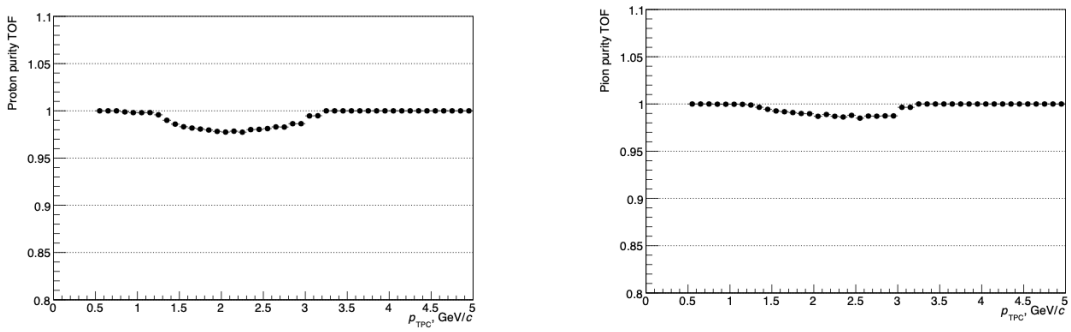

Figure 30: Purity of proton (left) and pion (right) samples estimated in the TOF detector

3.4 TOF/TPC Ratio for selected protons and pions

In order to investigate the loss of protons and pions between TOF and TPC detectors, the number of particles with matched TOF hit is compared to the number of particles reconstructed in the TPC detector. Such a ratio is investigated as a function of p_{TPC}, i. e. the momentum at the inner TPC wall. Due to energy loss effects in the ITS detector, this momentum can be different from the momentum p reconstructed at the V^0 decay vertex, which affects the ratio at low momenta (Fig. 31 illustrates the effect for protons). Therefore, the momentum p_{TPC} provides a uniform "starting point" for both MC and experimental data analyses and excludes any possible effects due to imperfect description of energy loss in MC simulations at very low momentum.

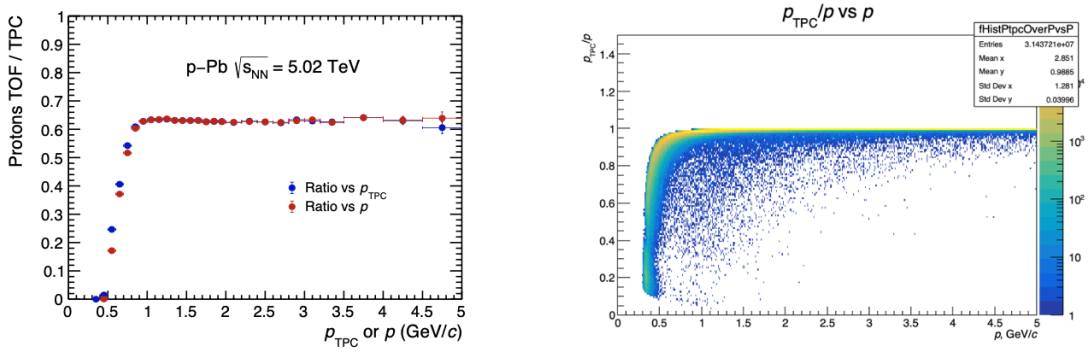

Figure 31: Purity of proton (left) and pion (right) samples estimated in the TOF detector

The resulting TOF/TPC ratio of protons from Λ decays is shown in Fig. 32. For charged pions from $\mathrm{K}^0_{\mathrm{S}}$ decays, Fig. 33 shows the results for both π^+ and π^-. Small differences observed between charged pions can be explained by slightly non-symmetrical acceptance of the ALICE detectors (the magnetic field polarity in analysed p–Pb data was always the same). Since this difference is very small, as can be seen in Fig. 33, from now on we will present the results for the case of π^+, since the ones for π^- are almost identical.

These ratios are obviously affected by the detector acceptance, the inelastic interactions and the material budget of the detector. However, the first two aspects can be well described in the MC simulations (the inelastic cross sections of hadrons in question are known from experiment), which allows us to study the material budget with this observable.

All these ratios will be compared to the results from MC simulations in Section 5.

3.5 Monte Carlo Analysis

For the validation of the TRD material budget the experimental ratios shown in Figs. 32 and 33 are compared to the results from detailed Monte Carlo simulations. To this purpose, in Monte Carlo data the decays of $\Lambda \to \mathrm{p} + \pi^-$ and $\mathrm{K}^0_{\mathrm{S}} \to \pi^+ + \pi^-$ are pre-selected on the generator level using the PDG codes of mother and daughter particles. After this selection, the same V^0 selection criteria as listed in Table 2 are applied to reconstructed Monte Carlo data. Figs. 34 and 35 show the comparison of Λ distributions in experimental data and in Monte Carlo analysis, and Figs. 36 and 37 the comparison for $\mathrm{K}^0_{\mathrm{S}}$. A good agreement between data and Monte Carlo can be seen for all variables, both for Λ and for $\mathrm{K}^0_{\mathrm{S}}$ decays.

The daughters of V^0 decays are also required to fulfil the same track and PID selection as applied to experimental data (Table 3). Since the processes in question $\Lambda \to \mathrm{p} + \pi^-$ and $\mathrm{K}^0_{\mathrm{S}} \to \pi^+ + \pi^-$ are pre-selected on generator level, in Monte Carlo simulations no contamination

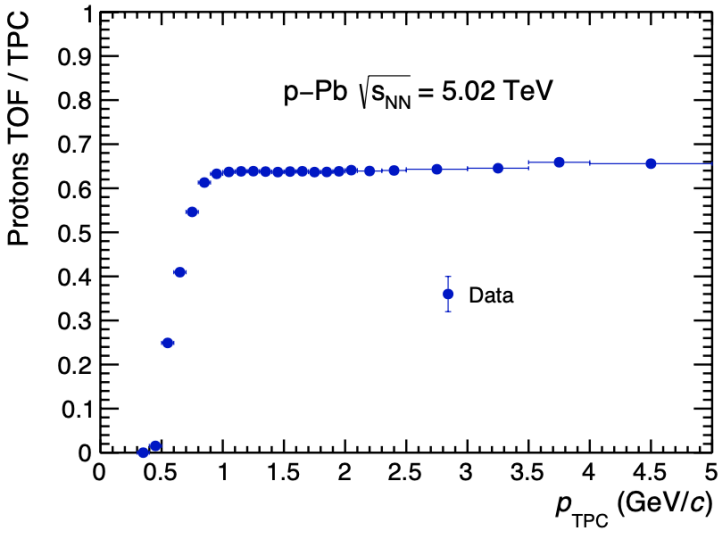

Figure 32: TOF/TPC ratio of protons from Λ decays in experimental data. Only statistical uncertainties are shown.

is presented in the final sample of protons and pions (Figs. 38-40) by construction.

Since in Monte Carlo data one can also select pure *primary* protons and pions using their PDG codes, the absorption of these primary particles in the TRD has been compared to the one of secondary protons and pions from V^0 decays. Fig. 42 shows this comparison for primary and secondary protons in MC GEANT3 simulations, and Fig. 43 the same comparison for π^+. As expected, the resulting TOF/TPC ratio is very similar for primary and secondary particles, so that in first approximation the loss of particles in the TRD material does not depend on their origin. However, small difference of up to 2% can be seen in Figs. 42 and 43, which can come from slightly different $\eta - \phi$ distributions of primary and secondary particles. These distributions are shown for experimental (secondary) protons and for primary and secondary protons in MC in Fig. 44. One can clearly see some distinct $\eta - \phi$ structure for secondary protons, which is well reproduced in Monte Carlo simulations. Such a structure most probably comes from the track requirements used in the analysis (at least 2 ITS hits), which are convoluted with imperfect coverage of outer ITS layers. Since Λ particles have $c\tau = 7.89\ cm$, in this analysis 48% of Λ candidates have a decay point beyond the first SPD layer and 22% beyond the second SPD layer (the values are obtained from the distribution in Fig. 16), which makes this effect more pronounced in the $\eta - \phi$. Due to slightly different resulting $\eta - \phi$ distributions, primary and secondary protons can therefore cross slightly different parts of the ALICE detector material. For this reason, for the comparison between data and Monte Carlo secondary protons from Λ decays are used both in experimental data and in MC. For pions the differences in $\eta - \phi$ distributions are less pronounced (Fig. 45). The decays of K^0_S particles happens closer to the primary event vertex ($c\tau = 2.86\ cm$, with 31% of K^0_S having decay point beyond first and 10% beyond second SPD layer in this analysis (Fig. 19), so the daughter pion tracks often have whole ITS detector at their disposal. However, also in this case a difference of up to 2% is observed between the absorption of primary and secondary pions, so for consistency the results from data and Monte Carlo are compared in Section 5 using secondary pions from K^0_S decays in both cases.

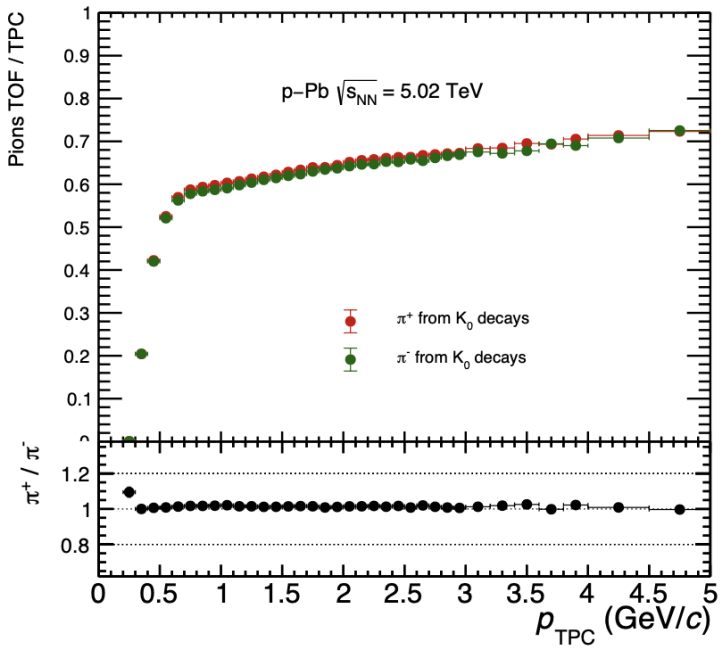

Figure 33: TOF/TPC ratio of charged pions from K^0_S decays in experimental data. Only statistical uncertainties are shown.

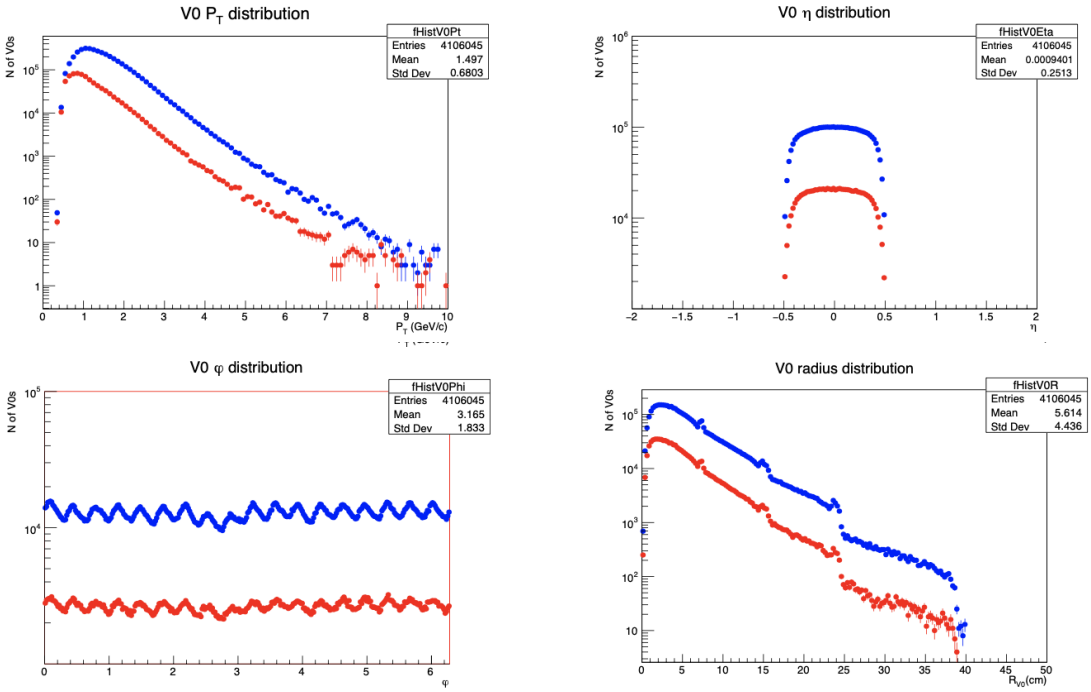

Figure 34: p_t, η, φ and decay radius distributions of selected Λ candidates in experimental data (blue) and Monte Carlo analysis (red).

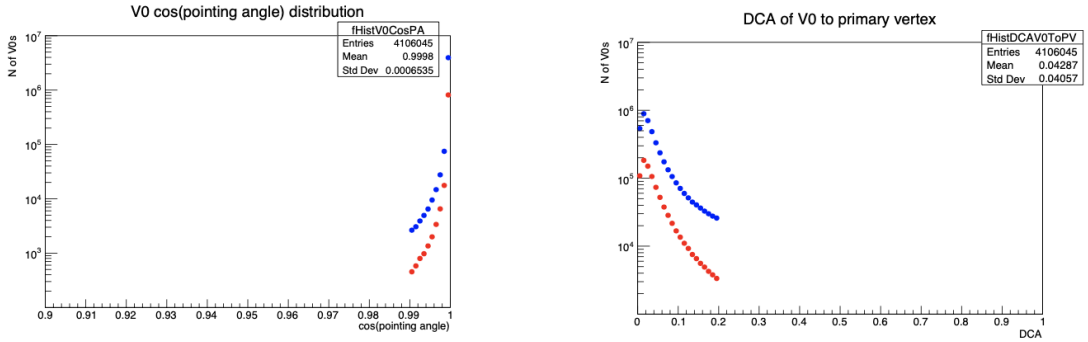

Figure 35: Cosine of pointing angle and DCA to primary vertex of selected Λ candidates in experimental data (blue) and Monte Carlo analysis (red).

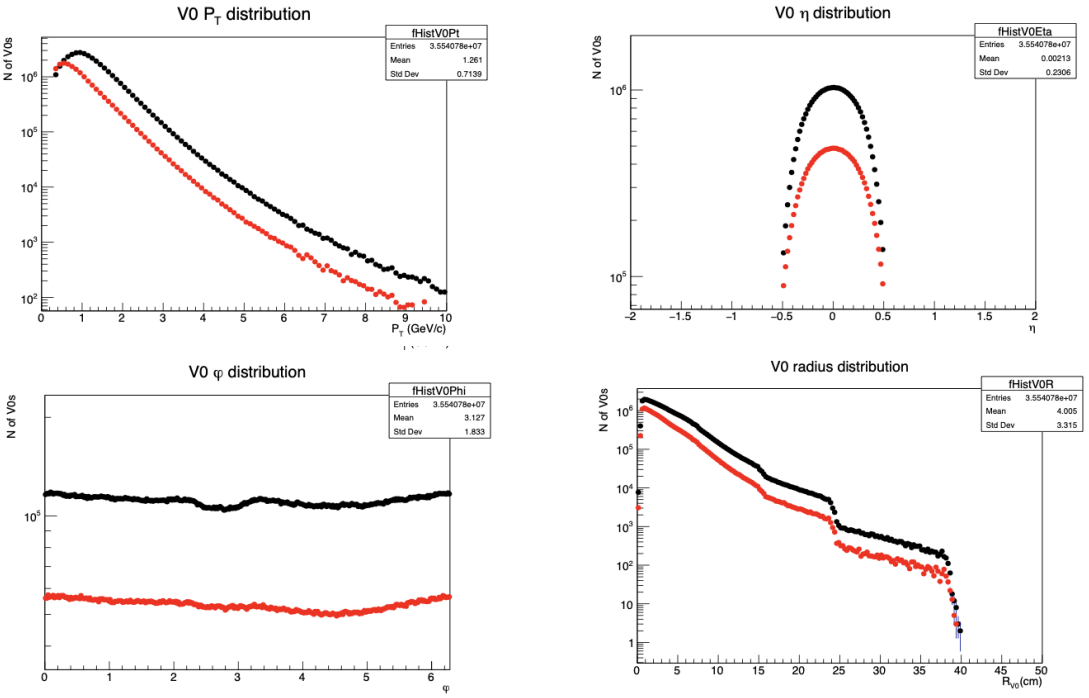

Figure 36: p_t, η, φ and decay radius distributions of selected K^0_S candidates in experimental data (black) and Monte Carlo analysis (red).

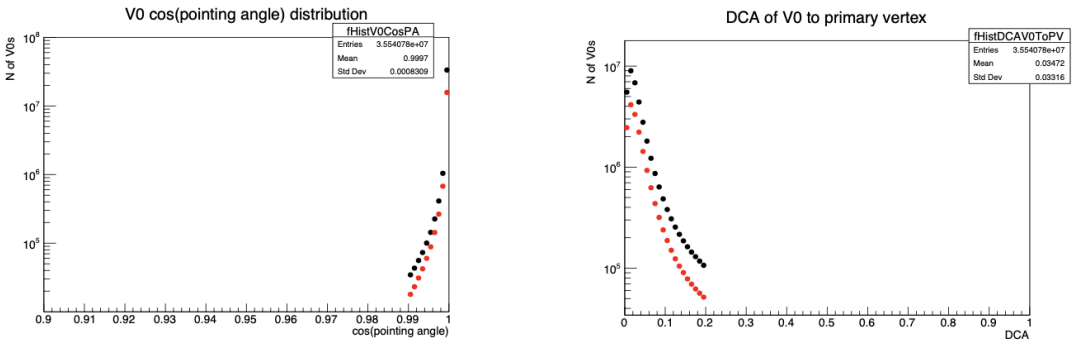

Figure 37: Cosine of pointing angle and DCA to primary vertex of selected K^0_S candidates in experimental data (black) and Monte Carlo analysis (red).

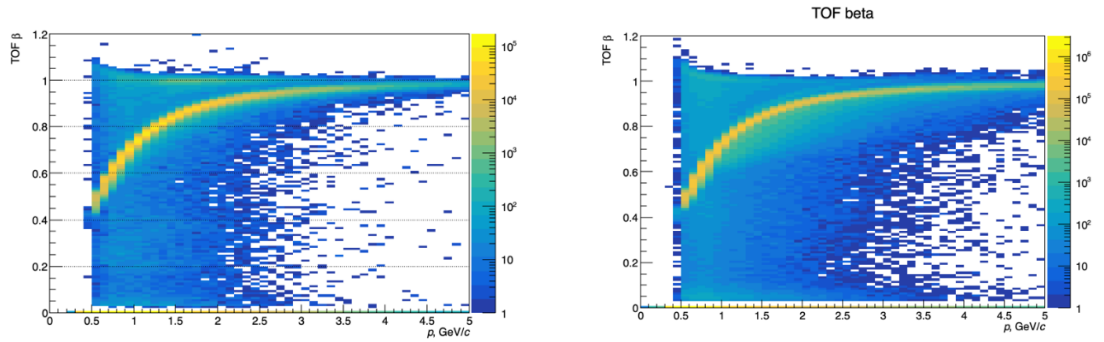

Figure 38: TOF β as a function of momentum p for selected protons in experimental data (left) and Monte Carlo analysis (right).

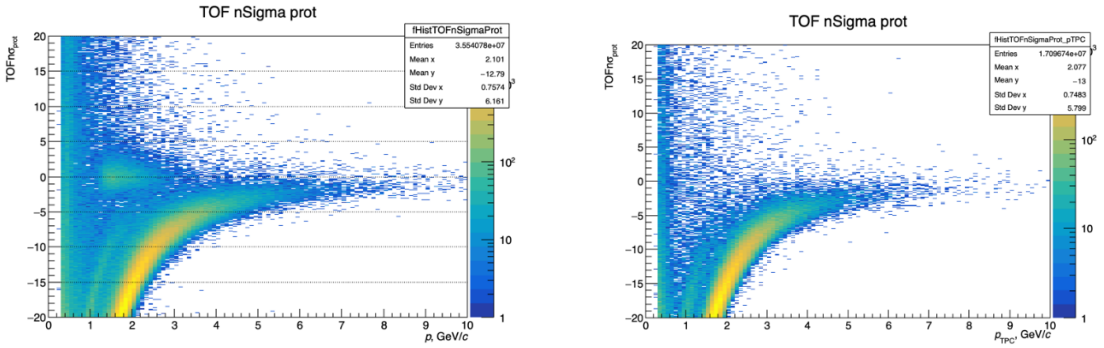

Figure 39: TOF$n\sigma(proton)$ as a function of momentum for selected protons in experimental data (left) and Monte Carlo analysis (right).

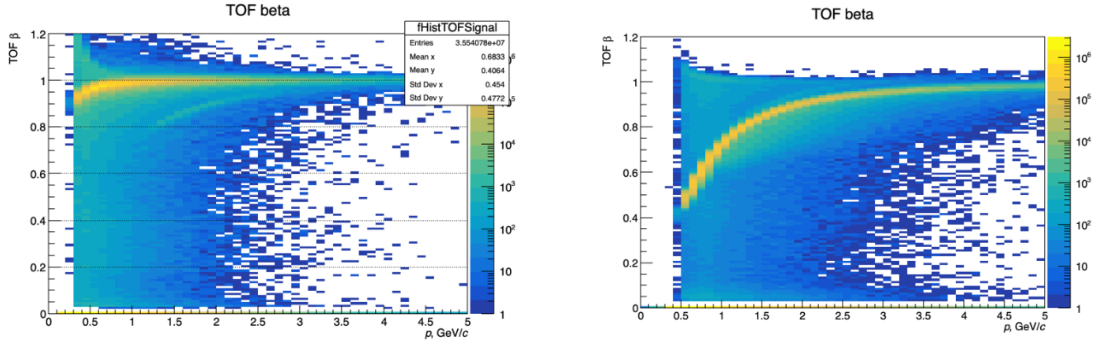

Figure 40: TOFβ as a function of momentum for selected pions in experimental data (left) and Monte Carlo analysis (right).

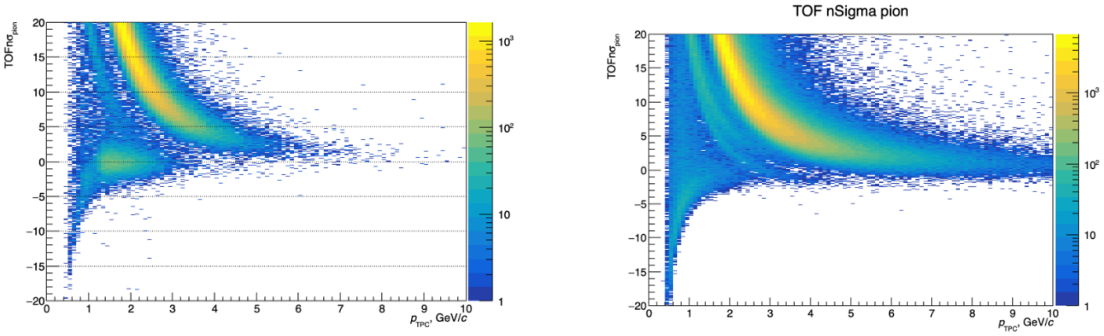

Figure 41: TOF$n\sigma(pion)$ as a function of momentum for selected pions in experimental data (left) and Monte Carlo analysis (right).

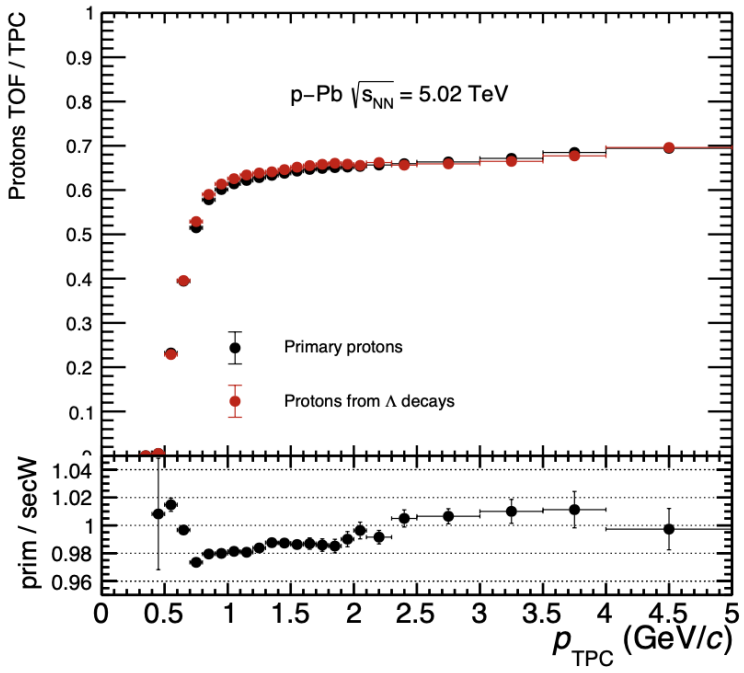

Figure 42: TOF/TPC ratio of protons from Λ decays and of primary protons in MC data (GEANT3). Only statistical uncertainties are shown.

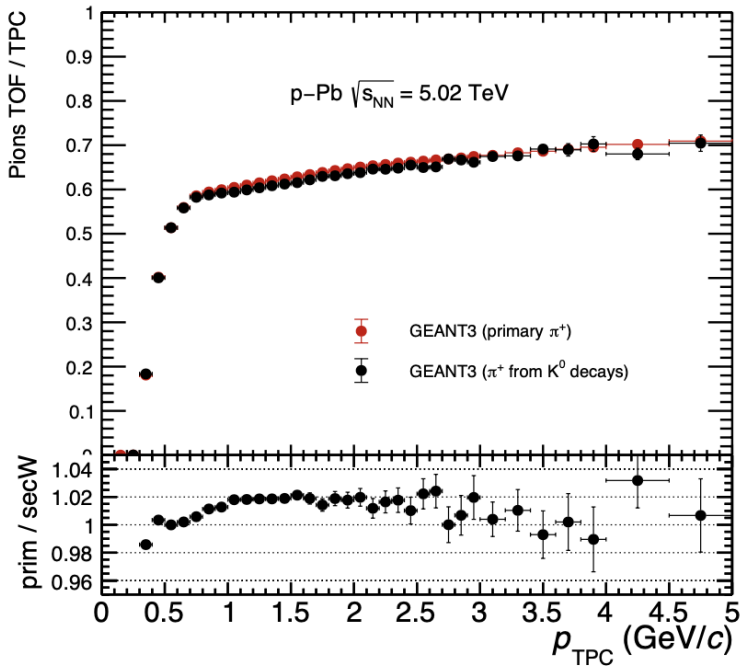

Figure 43: TOF/TPC ratio of pions from K^0_S decays and of primary pions in MC data (GEANT3). Only statistical uncertainties are shown.

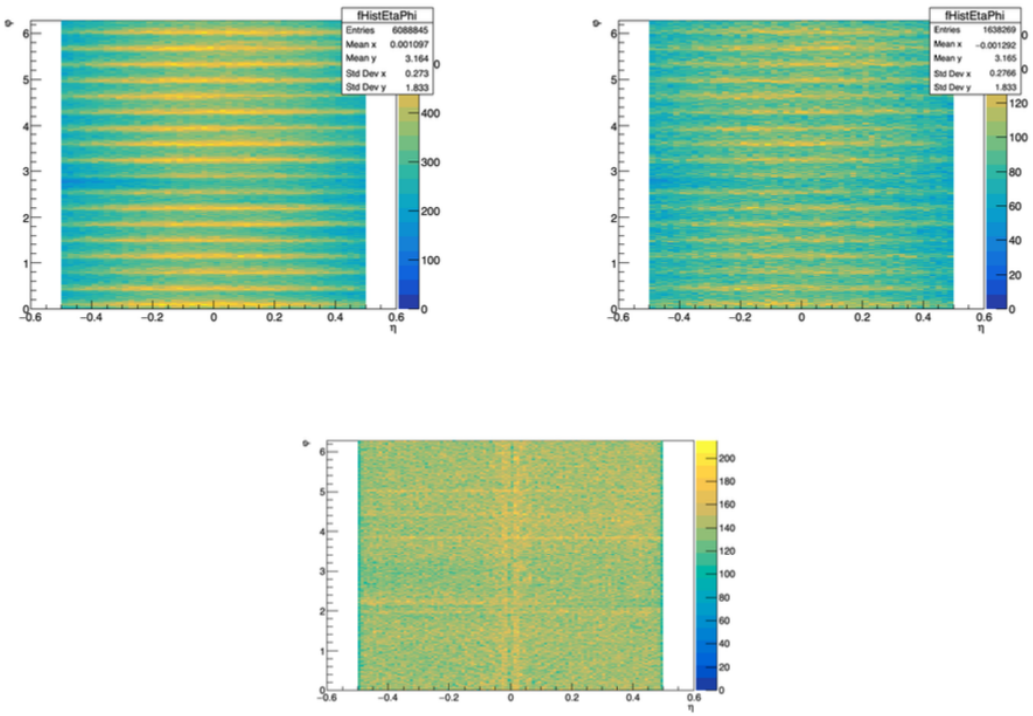

Figure 44: $\eta - \phi$ distributions of secondary protons in data (left) and in Monte Carlo (middle) and of primary protons in Monte Carlo (right).

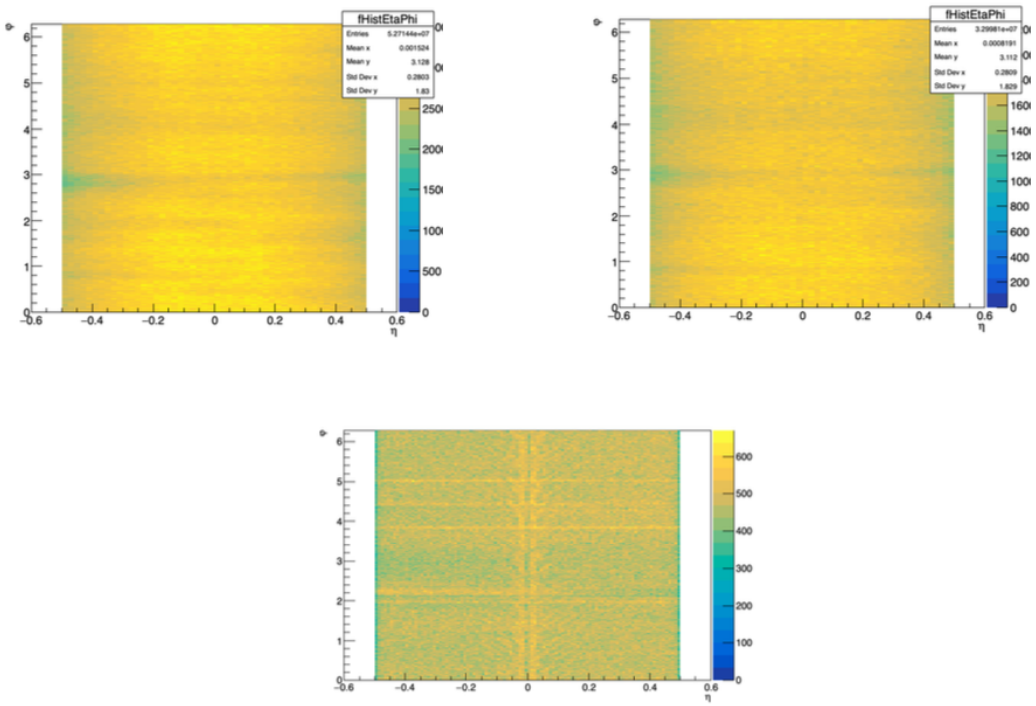

Figure 45: $\eta - \phi$ distributions of secondary pions in data (left) and in Monte Carlo (middle) and of primary pions in Monte Carlo (right).

4 Systematic Checks and Uncertainties

This Chapter describes various checks which have been done in order to estimate any systematic bias in the final results and, if needed, to assign the corresponding uncertainties. The following sources of systematic uncertainties have been investigated for the analysis and are described in more details below:

- V^0 and track selection criteria listed in Tables 2 and 3
- Mass and q_t selection criteria listed in Table 2
- Contamination of final samples of protons and pions
- Variation of inelastic cross sections of protons and pions within the agreement between experimental data and GEANT parameterisations

4.1 V^0 and track selection criteria

In order to investigate the systematic uncertainty due to V^0 and track selection criteria used in the analysis, the values listed in Tables 2 and 3 have been varied between loose, default and tight ones as shown in Table 4. The values are chosen in such a way that the variations in the statistics of final pion and proton samples are $15 - 25\%$ with respect to the default case.

Table 4: Variations of V^0 and track selection criteria

Variable	Loose	Default	Tight
V^0 pseudorapidity	$\|\eta\| < 0.55$	$\|\eta\| < 0.5$	$\|\eta\| < 0.45$
V^0 transverse momentum	$p_{\mathrm{t}} > 0.2\,\mathrm{GeV}/c$	$p_{\mathrm{t}} > 0.3\,\mathrm{GeV}/c$	$p_{\mathrm{t}} > 0.4\,\mathrm{GeV}/c$
V^0 decay radius	$0.1 < r_{xy} < 50$ cm	$0.2 < r_{xy} < 40$ cm	$0.3 < r_{xy} < 35$ cm
V^0 pointing angle	$\cos\phi > 0.98$	$\cos\phi > 0.99$	$\cos\phi > 0.995$
DCA of V^0 to prim. vertex	DCA < 0.4 cm	DCA < 0.3 cm	DCA < 0.2 cm
Track Pseudorapidity	$\|\eta\| < 0.55$	$\|\eta\| < 0.5$	$\|\eta\| < 0.45$
N of TPC Clusters	≥ 65	≥ 80	≥ 100
N of ITS Clusters	≥ 1	≥ 2	≥ 2
DCA to primary Vertex	$\mathrm{DCA}_{xy} > 0.03cm$	$\mathrm{DCA}_{xy} > 0.05cm$	$\mathrm{DCA}_{xy} > 0.07cm$
PID Selection	$\|\mathrm{TPCn}\sigma\| < 3.5$	$\|\mathrm{TPCn}\sigma\| < 3.0$	$\|\mathrm{TPCn}\sigma\| < 2.5$

The analysis has been repeated for these 3 sets of selection criteria, both in experimental data and in Monte Carlo simulations, and the data/MC ratios have been checked in large momentum bins in order to suppress the statistical uncertainties. Fig. 46 shows the resulting deviations in data/MC ratios for pions and protons. The maximal deviation with respect to the default case seen in the bottom panels is taken into account as a systematic uncertainty. Since for protons the results from loose and tight selections are in agreement with the default case within (large) statistical uncertainties above $p = 1.0$ GeV/c, in this momentum range the corresponding systematic uncertainty for protons is taken from pions $(0.6 - 0.9\%)$

4.2 Mass and q_t selection criteria

In addition to the variations of V^0 and track selection, also the mass and q_t selection criteria are considered as a source of systematic uncertainty for this analysis. Table 5 summarises 3 sets of

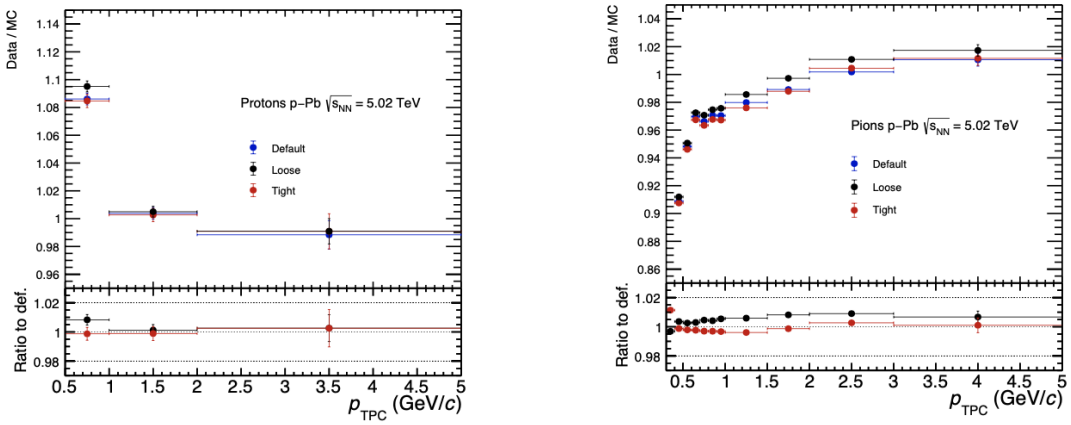

Figure 46: Data/MC ratios for 3 different set of V^0 and track cuts for protons (left) and pions (right). Bottom panels show the deviations with respect to the default settings.

varied mass and q_t selection criteria which change the statistics of final pion and proton samples by about $15-20\%$. Note that loose selection or rejection of Λ candidates is combined with tight rejection or selection of K^0_S particles. Therefore, "Variation 1" case corresponds to higher purity of Λ and lower purity of K^0_S candidates, whereas "Variation 2" corresponds to the case of lower Λ and higher K^0_S purities. The analysis has been repeated in data and in Monte Carlo for all 3 cases, and the resulting data/MC ratios are shown in Fig. 47. Once again, maximal deviation with respect to the default case, if it's significant, is taken into account as systematic uncertainty.

Table 5: Variations of mass and q_t selection criteria

Mother particle	Variation 1	Default	Variation 2
Λ	$1.113 < m_{p\pi} < 1.119$ GeV/c^2 $0.025 < q_t < 0.105$ GeV/c^2	$1.112 < m_{p\pi} < 1.120$ GeV/c^2 $0.02 < q_t < 0.11$ GeV/c	$1.111 < m_{p\pi} < 1.121$ GeV/c^2 $0.015 < q_t < 0.12$ GeV/c
K^0_s	$0.47 < m_{\pi\pi} < 0.525$ GeV/c^2 $q_t > 0.105$ GeV/c	$0.48 < m_{\pi\pi} < 0.515$ GeV/c^2 $q_t > 0.11$ GeV/c	$0.485 < m_{\pi\pi} < 0.51$ GeV/c^2 $q_t > 0.12$ GeV/c

4.3 Contamination

Small contamination shown in Fig. 30 can in principle change the resulting TOF/TPC ratios of pions and protons. To estimate the effect of this contamination, a pure TOF/TPC ratio has been estimated in the following way and compared to the contaminated ratio. To this purpose, let's consider the TOF/TPC ratio for protons contaminated with pions, which can be written in the following way:

$$\frac{N^{TOF}_{all}}{N^{TPC}_{all}} = \frac{N^{TOF}_{prot} + N^{TOF}_{pion}}{N^{TPC}_{prot} + N^{TPC}_{pion}} \tag{5}$$

Here the number of protons and pions in TOF is $N^{TOF}_{prot} = N^{TOF}_{all} \times P^{TOF}_{prot}$ and $N^{TOF}_{pion} = N^{TOF}_{all} \times (1 - P^{TOF}_{prot})$, correspondingly, with P^{TOF}_{prot} being the purity of protons estimated with TOF (Fig. 30 left). Since we know the absorption of pions and their TOF/TPC ratio, one can also estimate the number of pions which are present in the TPC sample as:

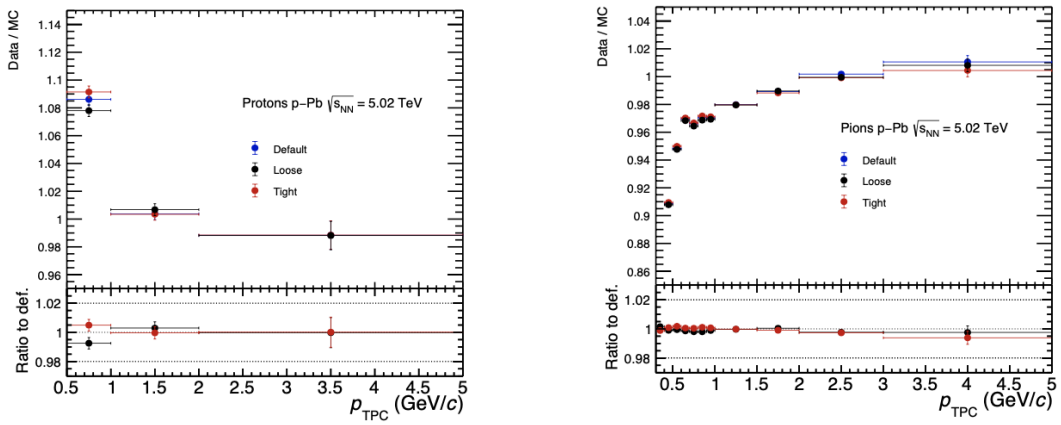

Figure 47: Data/MC ratios for 3 different set of mass and q_t selection criteria for protons (left) and pions (right). Bottom panels show the deviations w.r.t. default case.

$$N_{pion}^{TPC} = N_{pion}^{TOF} \times \frac{N_{pion}^{TPC}}{N_{pion}^{TOF}} = N_{pion}^{TOF} \times \frac{1}{R_{pion}} \tag{6}$$

Note that R_{pion} here is "contaminated" TOF/TPC ratio for pions (Fig. 33), but this second-order effect can be safely neglected. The number of pure protons in the TPC is then $N_{prot}^{TPC} = N_{all}^{TPC} - N_{pion}^{TPC}$ and so one can construct the pure TOF/TPC ratio for protons as:

$$\frac{N_{prot}^{TOF}}{N_{prot}^{TPC}} = \frac{N_{all}^{TOF} \times P_{prot}^{TOF}}{N_{all}^{TPC} - N_{all}^{TOF} \times (1 - P_{prot}^{TOF}) \times (\frac{1}{R_{pion}})} \tag{7}$$

The same logic (but inverted between pions and protons) can be applied to pions contaminated by protons to get pure TOF/TPC ratio for pions. Fig. 48 shows the comparison between contaminated TOF/TPC ratios and the pure ones estimated in this way for protons and pions. One can see that the resulting deviations are very small, reaching 0.1 % at maximum.

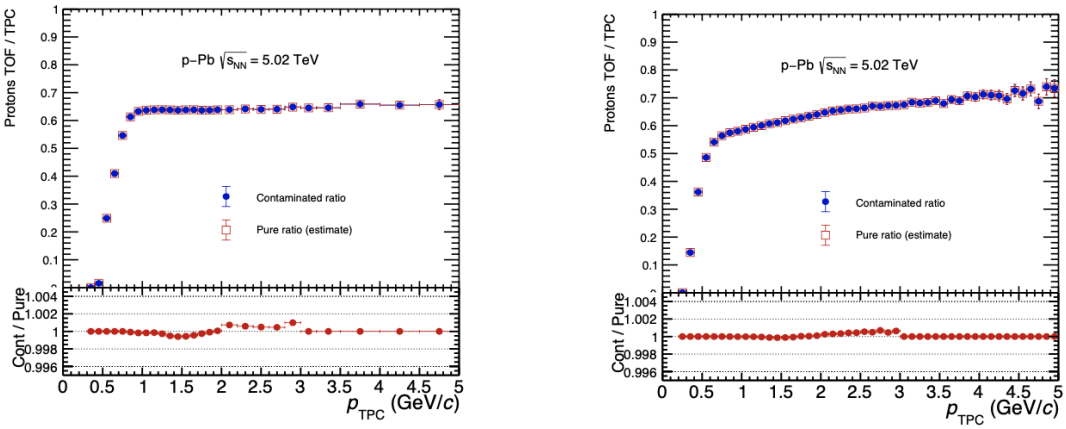

Figure 48: Comparison of contaminated and pure TOF/TPC ratios for protons (left) and pions (right).

For the proton analysis another source of possible contamination can be considered, namely,

if the contamination comes actually not from pions, but from electrons originating from photon conversions and misidentified as pions in the TOF. In order to check the effect of such assumption, the TOF/TPC ratio for electrons R_{ele} has been calculated in the experimental data using electrons from photon conversions. The selection criteria listed in Table 2 have been adjusted in order to select photon conversions in the detector material (no cuts on invariant mass plus $q_t < 0.01\,\mathrm{GeV}/c$ requirement), and the daughter tracks of electrons and positrons have been selected with the selection criteria listed in Table 3 using $|\mathrm{TPC}_{\mathrm{n}\sigma\mathrm{ele}}| < 3$, which can be seen in Fig. 49

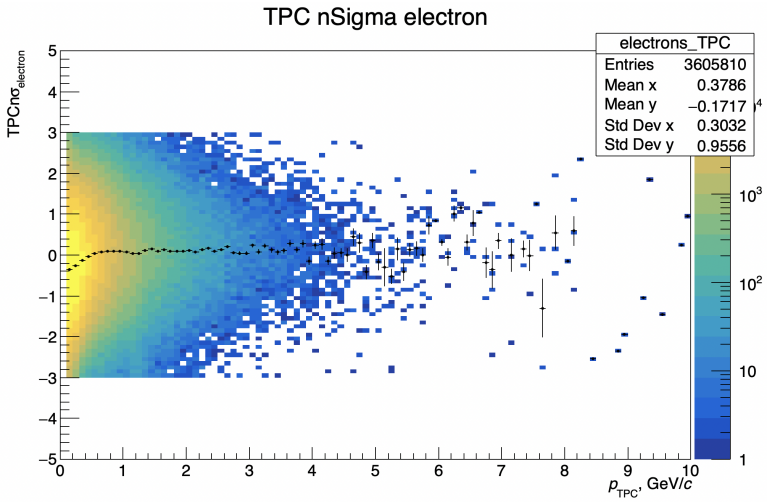

Figure 49: TPC$n\sigma$(electron) for electron candidates from photon conversions. Black points show mean TPC$n\sigma$(electron) value in each momentum bin.

Pure TOF/TPC ratio has been constructed for protons in the same way as described above, but replacing R_{pion} with R_{ele} (Fig. 50 left). The results are shown in Fig. 50 (right), where a difference of up to $\sim 0.04\%$ can be seen. This difference has been added in quadrature to the total systematic uncertainty for the final results.

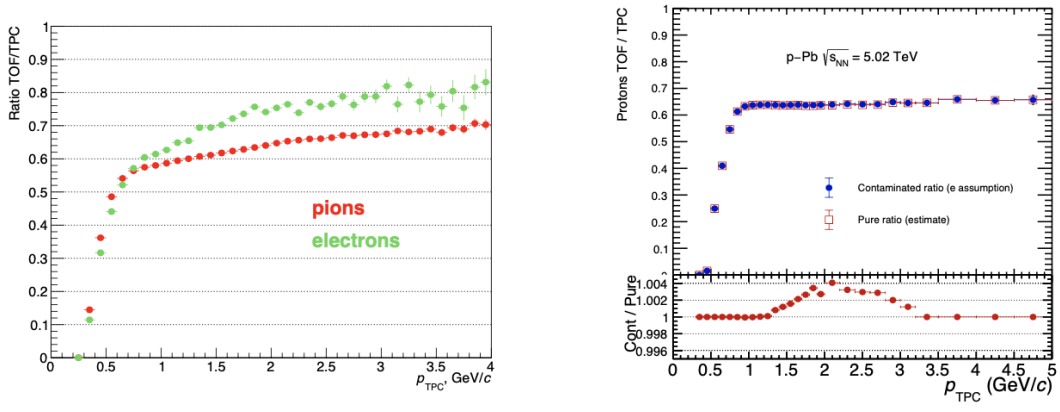

Figure 50: Left: TOF/TPC ratio in experimental data for pion from K^0_S decays and for electrons from photon conversions. Right: comparison of contaminated and pure TOF/TPC ratios for protons under assumption that all contamination comes from electrons.

4.4 Inelastic cross section of pions and protons

Precise knowledge of inelastic cross sections of protons and pions with matter is a key aspect of this analysis. In order to estimate the corresponding impact on the TOF/TPC ratio, the pion and proton inelastic cross sections have been varied in MC simulations by the uncertainty obtained from fits of GEANT parameterisations to various experimental data [48–52] as described in the following. The parameterisations implemented in the GEANT4 toolkit relies on Barashenkov data set as described in [47], whereas GEANT3 simulates hadronic interactions of charged pions and protons with the detector material according to the cross sections implemented in the GHEISHA package [46, 53].

Fig. 51 shows the comparison between the experimental data for proton inelastic cross sections on various materials with parameterisations employed in GEANT. The overall agreement between the GEANT4 parameterisations and the available measurements has been quantified by shifting the GEANT4 parameterisations up and down by some factor and calculating the χ^2/NDF value for each trial (Fig. 51 right). The minimum χ^2 value (i.e. the best agreement) is achieved for the factor of 0.993. The $\pm 1\sigma$ deviations correspond to the change in χ^2/NDF value by 1.0 [54], which leads to the uncertainty of 0.035 on this re-scaling factor.

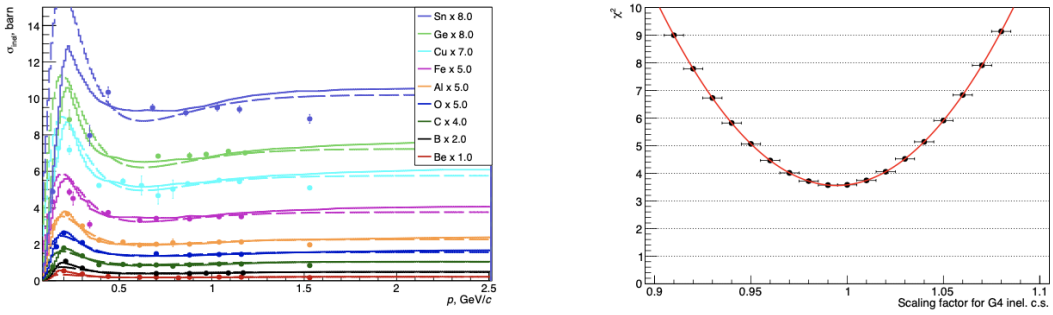

Figure 51: Left: experimental inelastic proton–nucleus cross sections compared to the GEANT3 (dashed lines) and GEANT4 (full lines) parameterisations. Right: χ^2/NDF as a function of the re-scaling factor for GEANT4 parameterisations used in the combined fit.

Following these results, the inelastic cross section of protons have been changed by $\pm 3.5\%$ in simple GEANT4-based Monte Carlo simulations (taken from [55]) to see the effect on TOF/TPC ratio. In these simple simulations the TRD detector was represented as a stack of materials, with a thickness corresponding to the average value for each of the materials that can be found in 1. For each value of the inelastic cross section, 5×10^6 protons with flat kinetic energy distribution have been shot onto such a target, and the proton momentum spectra are checked before and after the target. Fig. 52 (left) shows schematically the experimental setup used for this check. The resulting changes in the proton spectrum after the target ($\sim 0.5\%$) are shown in Fig. 52 (right) and are assigned to the final results as a systematic uncertainty.

In the same way the pion inelastic cross section have been studied as well, and the experimental data taken from [48] can be well described by the GEANT4 parameterisations (Fig. 53). The minimum χ^2 value obtained in the same way as for protons is achieved for the scaling factor of 1.08, and the $\pm 1\sigma$ deviations correspond to additional variations of ± 0.06 on this factor.

Following these results, the inelastic cross section of pions has been changed by $+14\%$ in simple GEANT4-based Monte Carlo simulations to see the effect on "TOF/TPC" ratio. As for protons, 5×10^6 pions with flat kinetic energy distribution have been shot onto this target. The resulting change in the pion spectrum after the target is shown in Fig. 54; the corresponding uncertainty of 1.6% is assigned to the final pion results.

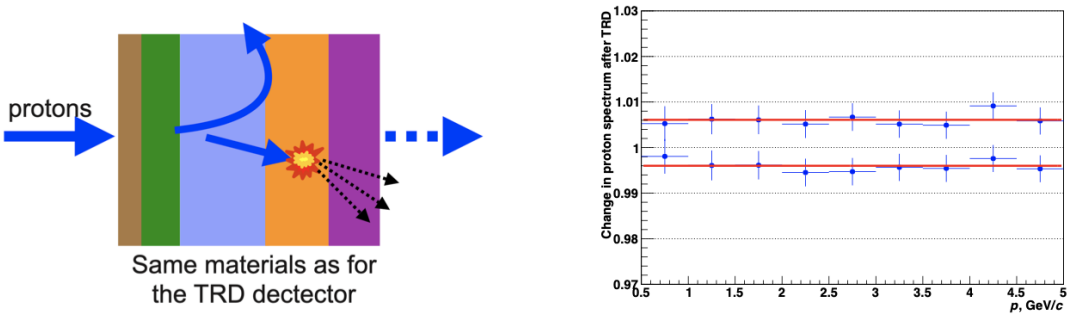

Figure 52: Left: schematic illustration of simple GEANT4-based Monte Carlo simulations used for the studies of systematic uncertainty due to proton σ_{inel}. Right: change in proton spectrum after the target due to variations of proton inelastic cross section.

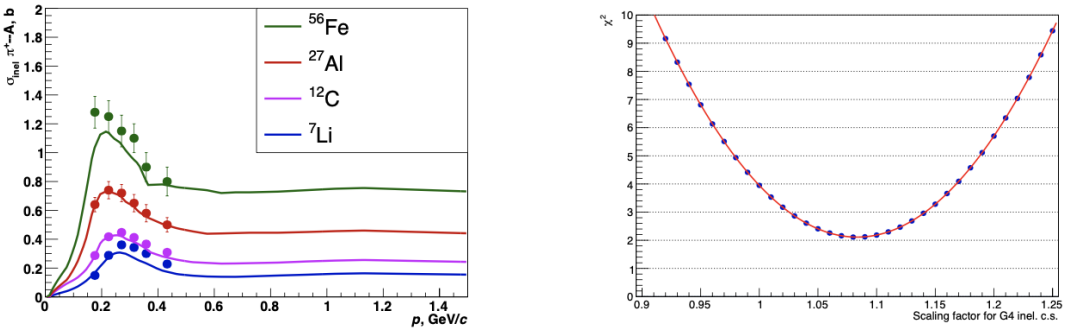

Figure 53: Left: experimental inelastic pion–nucleus cross sections from [48] compared to the GEANT4 parameterisations. Right:χ^2/NDF as a function of the re-scaling factor used in the combined fit

4.5 Total systematic uncertainties

The systematic uncertainties from individual sources described in this Section have been added in quadrature and are assigned to experimental data points and data/MC ratios for the results shown in Section 5.

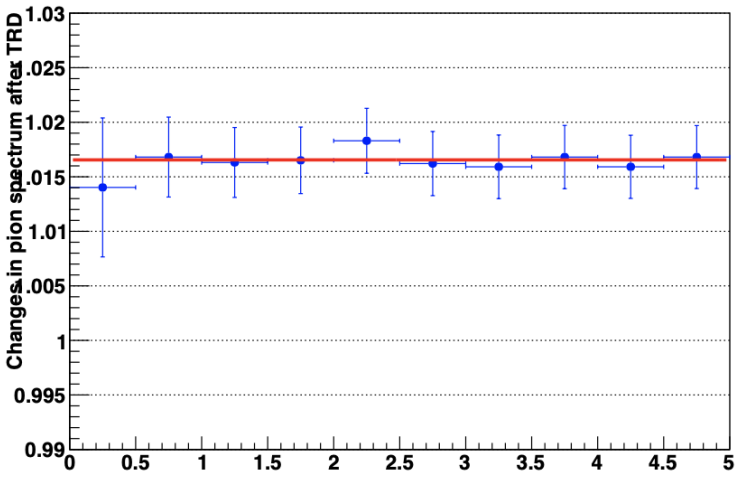

Figure 54: The change in pion spectrum after the target due to variations of pion inelastic cross section

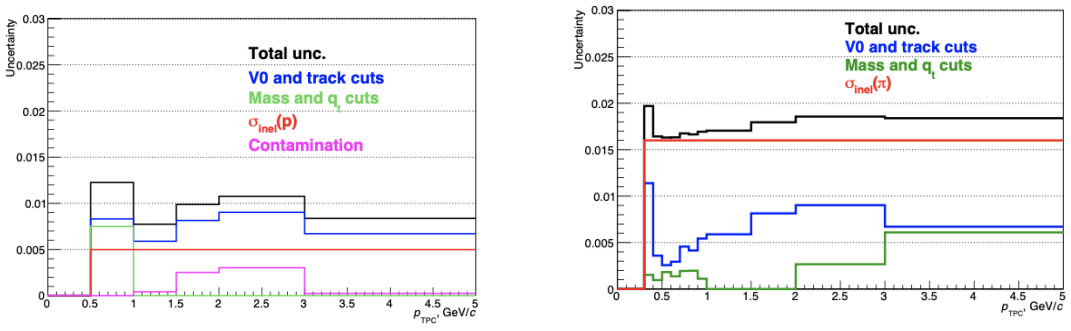

Figure 55: Total systematic uncertainties for proton (left) and pion (right) results.

5 Results

Fig. 56 shows the comparison of TOF/TPC ratio for protons between experimental data and Monte Carlo results taking into account the uncertainties explained in Section 4. A good overall agreement between experimental data and Monte Carlo simulations can be observed in the whole investigated momentum range. From this one can confirm that the material budget between TPC and TOF is in general well described in Monte Carlo simulations. The same conclusion can be obtained for pions from Fig. 57.

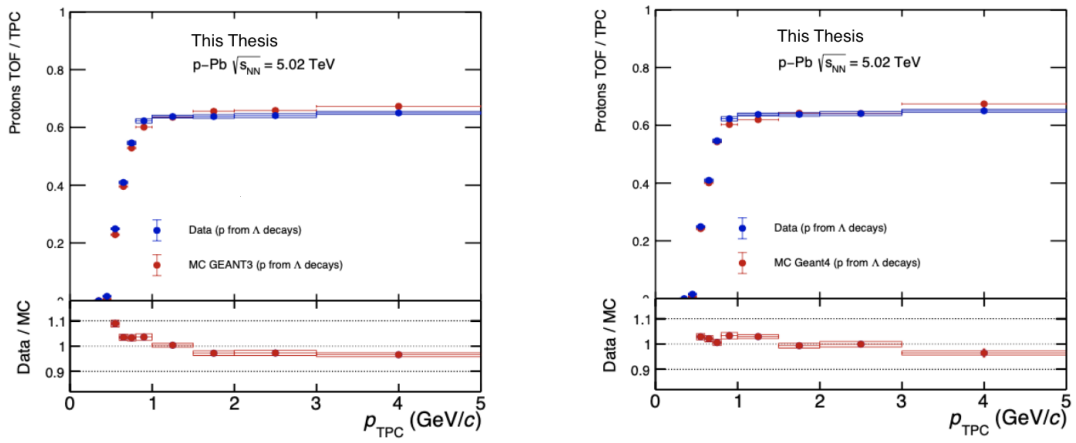

Figure 56: TOF/TPC ratio of protons in experimental data compared to the results in MC: GEANT3 (left) and GEANT4 (right).

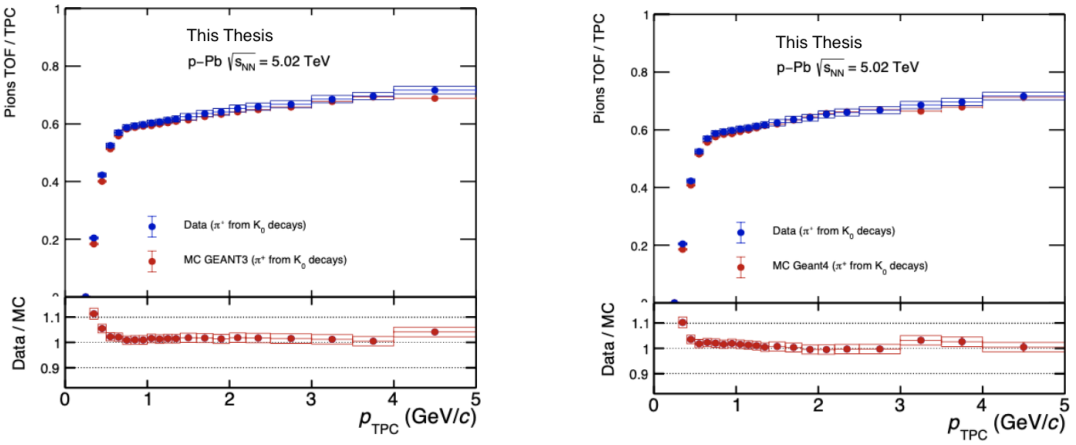

Figure 57: TOF/TPC ratio of pions in experimental data compared to the results in MC: GEANT3 (left) and GEANT4 (right).

One can use the ratio between experimental data and Monte Carlo simulations shown in the bottom panels of Fig. 56 and Fig. 57 to obtain the uncertainty related to the material budget between TPC and TOF. The data/MC ratio r can be expressed as:

$$r = \frac{e^{-\Delta x^{data}_{TOF-TPC}/\lambda_l}}{e^{-\Delta x^{MC}_{TOF-TPC}/\lambda_l}} = e^{-(\Delta x^{data}_{TOF-TPC} - \Delta x^{MC}_{TOF-TPC})/\lambda_l}. \quad (8)$$

Here, λ_l is the hadronic interaction length and $\Delta x^{data}_{TOF-TPC}$ and $\Delta x^{MC}_{TOF-TPC}$ are the thickness of the detector material between TOF and TPC detectors in experiment and in MC simulations correspondingly. The hadronic interaction length λ_l depends only on the material density and the inelastic cross section, and one can assume that these quantities are the same in data and in MC. Therefore, the corresponding uncertainty on the material between TPC and TOF $\Delta_{TOF-TPC}$ relative to the hadronic interaction length can be expressed as:

$$\Delta_{TOF-TPC} = \frac{\Delta x^{data}_{TOF-TPC} - \Delta x^{MC}_{TOF-TPC}}{\lambda_l} = -\ln(r). \tag{9}$$

Fig. 58 shows the resulting uncertainty $\Delta_{TOF-TPC}$ extracted from protons and pions in this way. For these results, in each momentum bin two values of r are considered ($r \pm 1\sigma$, where σ represents statistical and systematic uncertainties on r added in quadrature). Therefore the $\Delta_{TOF-TPC}$ is represented as a band in Fig. 58, with the width of the band corresponding to the total uncertainty from experimental data. As it can be seen from this Figure, both for GEANT3 and for GEANT4 Monte Carlo the uncertainty on the material budget between TOF and TPC amounts to $\lesssim 5\%$ in essentially whole investigated momentum range. All the lines are shown once again together on one plot in Fig. 59.

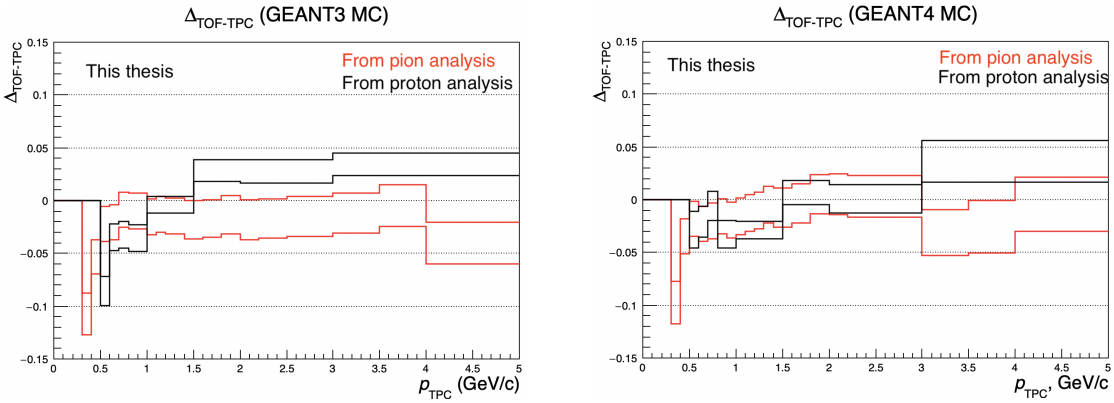

Figure 58: Uncertainty for the material budget between TPC and TOF extracted from protons (in black) and pions (in red) from Monte Carlo based on GEANT3 (left) and GEANT4 (right).

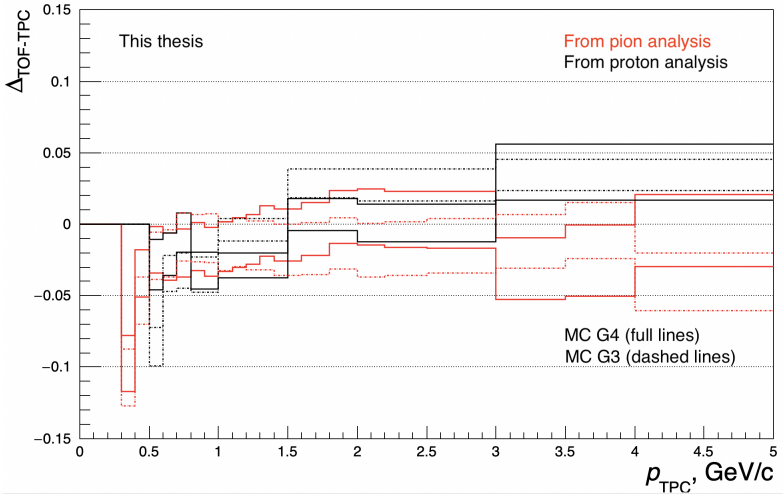

Figure 59: Uncertainty for the TRD material extracted from protons (in black) and pions (in red) from Monte Carlo based on GEANT3 (dashed lines) and GEANT4 (full lines).

Another possible way of representing the results is shown in Figures 60 and 61. In these figures the MC results are shown as a band, with a width of the band representing the uncertainty on the $\Delta_{TOF-TRD} = \pm 5\%$ calculated from the formulae above. This way the MC band covers the experimental results and their uncertainties in whole investigated momentum range.

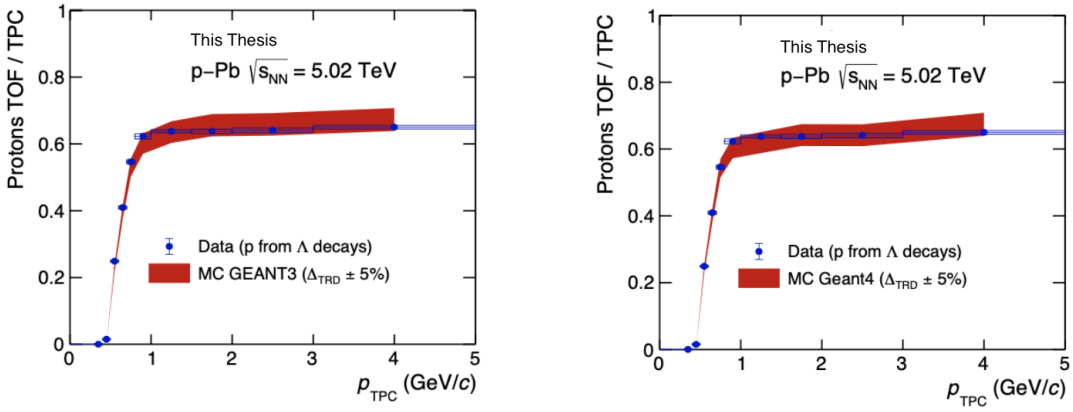

Figure 60: TOF/TPC ratio of protons(left) and pions(right) in experimental data compared to the results from GEANT3 MC. The width of the MC band represents the uncertainty on the $\Delta_{TOF-TPC} = \pm 5\%$.

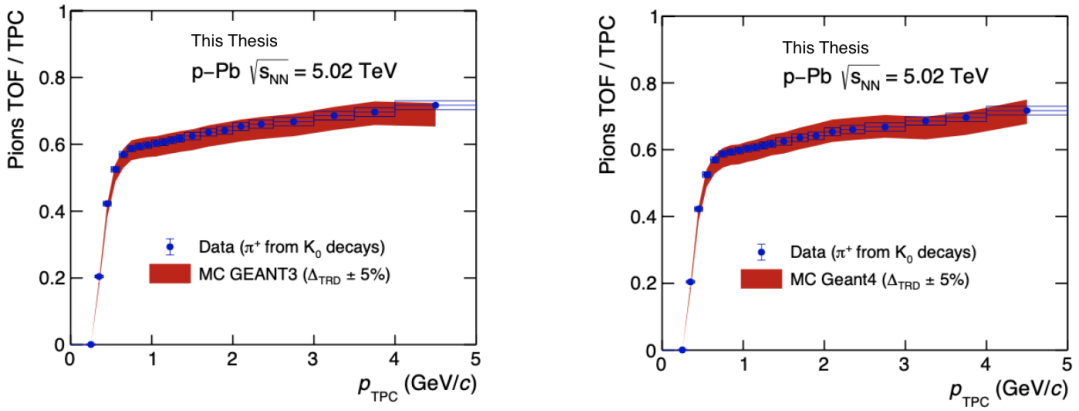

Figure 61: TOF/TPC ratio of protons(left) and pions(right) in experimental data compared to the results from GEANT4 MC. The width of the MC band represents the uncertainty on the $\Delta_{TOF-TPC} = \pm 5\%$.

The results presented in this thesis have been used in the analysis of $^3\overline{\text{He}}$ inelastic cross sections in Pb–Pb data at ALICE [39], for which the material budget between TPC and TOF detectors plays central role. The material budget has been varied by ±5.0%, and the corresponding impact on TOF/TPC ratio for $^3\overline{\text{He}}$ has been taken into account as a systematic uncertainty. The resulting uncertainty, together with other uncertainties estimated for that analysis, is shown in Fig. 62 as a function of $^3\overline{\text{He}}$ momentum. One can see that this uncertainty is not negligible, contributing significantly to the final results. At higher momentum the uncertainty due to material budget is compatible with those originating from track and PID selection of $^3\overline{\text{He}}$ and is even dominant in the two lowest momentum bins. The results on the $^3\overline{\text{He}}$ inelastic cross section obtained in [39] will be used in the future studies to calculate the expected $^3\overline{\text{He}}$ flux near Earth from DM and from cosmic ray collisions with interstellar medium.

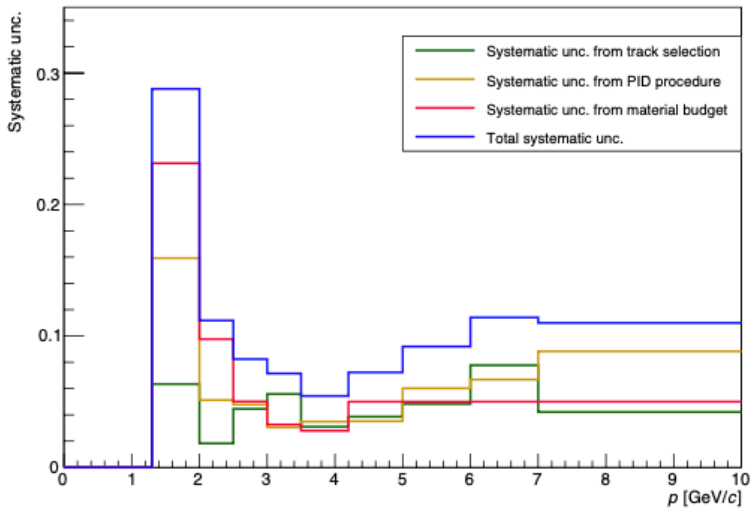

Figure 62: Summary of uncertainties for analysis of $^{3}\overline{\mathrm{He}}$ inelastic cross sections in ALICE [39]. The uncertainty due to material budget between TPC and TOF is shown in red.

6 Summary and Outlook

By using the experimental data from p–Pb collisions at $\sqrt{s_{\mathrm{NN}}} = 5.02$ TeV, we have been able to study how precisely the ALICE material budget between TPC and TOF is described in Monte Carlo simulations. For this purpose, the $\Lambda \longrightarrow \pi^- + p$ and $\mathrm{K}^0_{\mathrm{S}} \longrightarrow \pi^- + \pi^+$ decays have been used to obtain a pure sample of protons and pions. By comparing the number of hadrons which reached the TOF detector with the number of hadrons reconstructed in the TPC detector, the TOF/TPC ratios as a function of the momentum at the entrance of the TPC, $\mathrm{p_{TPC}}$, have been obtained for both protons and pions.

These ratios have been compared to the ones obtained from detailed Monte Carlo simulations based on GEANT3 and GEANT4 for particle's propagation through the detector, and a high level of agreement between experimental data and the simulations has been found. Therefore, in general the material budget in question is well described by the Monte Carlo simulations. Furthermore, we have used the ratio between the results to extract the uncertainty related to the detector material between TPC and TOF, which has been proven to be $\lesssim 5\%$. This is the first experimental check of this material budget in ALICE, which plays an important role for essentially all analyses employing detectors beyond the TPC, such as TOF, HMPID and EMCAL. The results presented in this thesis will be a part of the ALICE Public Note, which is currently under the internal collaboration review.

Further studies can be done in order to improve the knowledge of this material budget. More differential studies versus pseudorapidity η and azimuthal angle ϕ with high statistics obtained from pp collisions at 13 TeV can help to distinguish the contributions from the TRD detector itself and from the stainless–steel space frame surrounding the TPC. Another interesting study can be done by using the Run1 data collected in 2010-2013 when the TRD detector has been installed only partially - this would allow one to compare the TOF/TPC ratios with Monte Carlo simulations with and without the TRD material in between.

7 Appendix

Let us write down the transverse and longitudinal momentum of the particles in the CM frame, which we can get easily from fig. 14:

$$\begin{aligned} p_L^{cm} &= \pm p_{cm} \cdot \cos\theta \\ p_T^{cm} &= p_{cm} \cdot \sin\theta \end{aligned} \tag{10}$$

If one considers now the energy-momentum four vector, one can translate it to the laboratory frame using a Lorentz boost;

$$p_L = \gamma p_L^{cm} + \gamma\beta E^{cm} \tag{11}$$

Expressing the asymmetry in this longitudinal relativistic momentum:

$$\alpha = \frac{p_L^{(1)} - p_L^{(2)}}{p_L^{(1)} + p_L^{(2)}} \tag{12}$$

Substuting 11 into 12

$$\alpha = \frac{(p_{cm}\cos\theta + \beta E_1^{cm}) - (-p_{cm}\cos\theta + \beta E_2^{cm})}{(p_{cm}\cos\theta + \beta E_1^{cm}) + (-p_{cm}\cos\theta + \beta E_2^{cm}} = \frac{2p_{cm}\cos\theta + \beta(E_1^{cm} - E_2^{cm})}{\beta(E_1^{cm} - E_2^{cm})} \tag{13}$$

If energy-momentum conservation is applied, one gets the following relationships for E_1^{cm}, E_2^{cm}

$$\begin{aligned} E_1^{cm} &= \frac{1}{2M}(M^2 + m_1^2 - m_2^2) \\ E_2^{cm} &= \frac{1}{2M}(M^2 - m_1^2 + m_2^2) \end{aligned} \tag{14}$$

Therefore the difference between the energies of the two particles in the CM frame can be expressed as:

$$E_1^{cm} - E_2^{cm} = \frac{m_1^2 - m_2^2}{M} \tag{15}$$

One can now plug in equation 15 into 13, obtaining:

$$\alpha = \frac{2p_{cm}}{\beta M}\cos\theta + \frac{m_1^2 - m_2^2}{M^2} \tag{16}$$

The following structure can be obtained:

$$\begin{aligned} \alpha &= \alpha_0 + \frac{r_\alpha}{\beta}\cos\theta \\ \text{with } \alpha_0 &= \frac{m_1^2 - m_2^2}{M^2} \text{ and } r_\alpha = \frac{2p_{cm}}{M} \end{aligned} \tag{17}$$

If the relativistic limit is considered, $\beta \longrightarrow 1$ a relationship for $\cos\theta$ from equation 17 is obtained, and another for $\sin\theta$ using Eq. 10

$$\begin{aligned} \cos\theta &= \frac{\alpha - \alpha_0}{r_\alpha} \\ \sin\theta &= \frac{p_T}{p_{cm}} \end{aligned} \tag{18}$$

Using the known fundamental trigonometric equality to get the following relationship:

$$\frac{(\alpha - \alpha_0)^2}{r_\alpha^2} + \frac{p_T^2}{p_{cm}^2} = 1 \tag{19}$$

This is the equation of an ellipse. Therefore, if one represents these two variables $(\alpha, p_T)$of the decay particles in a plot, one should get the shape of an ellipse.

We can now get characteristic features of the ellipse which can allow us to differentiate between the different decays:

$$\text{Center of the ellipse, } (\alpha_0, 0) = (\frac{m_1^2 - m_2^2}{M^2}, 0) \tag{20}$$

$$\text{Radii of the ellipse, } (r_\alpha, r_{pT}) = (\frac{2p_{cm}}{M}, p_{cm}) \tag{21}$$

8 References

[1] F. Zwicky. "Die Rotverschiebung von extragalaktischen Nebeln". In: *Helv. Phys. Acta* 6 (1933), pp. 110–127. DOI: 10.1007/s10714-008-0707-4.

[2] Massimo Persic, Paolo Salucci, and Fulvio Stel. "The Universal rotation curve of spiral galaxies: 1. The Dark matter connection". In: *Mon. Not. Roy. Astron. Soc.* 281 (1996), p. 27. DOI: 10.1093/mnras/278.1.27. arXiv: astro-ph/9506004.

[3] J. R. Bond and G. Efstathiou. "Cosmic background radiation anisotropies in universes dominated by nonbaryonic dark matter". In: *Astrophys. J. Lett.* 285 (1984), pp. L45–L48. DOI: 10.1086/184362.

[4] P. de Bernardis et al. "A Flat universe from high resolution maps of the cosmic microwave background radiation". In: *Nature* 404 (2000), pp. 955–959. DOI: 10.1038/35010035. arXiv: astro-ph/0004404.

[5] Douglas Clowe et al. "A direct empirical proof of the existence of dark matter". In: *Astrophys. J. Lett.* 648 (2006), pp. L109–L113. DOI: 10.1086/508162. arXiv: astro-ph/0608407.

[6] N. Aghanim et al. "Planck 2018 results. VI. Cosmological parameters". In: *Astron. Astrophys.* 641 (2020). [Erratum: Astron.Astrophys. 652, C4 (2021)], A6. DOI: 10.1051/0004-6361/201833910. arXiv: 1807.06209 [astro-ph.CO].

[7] J. Silk et al. *Particle Dark Matter: Observations, Models and Searches*. Ed. by Gianfranco Bertone. Cambridge: Cambridge Univ. Press, 2010. ISBN: 978-1-107-65392-4. DOI: 10.1017/CBO9780511770739.

[8] Jehanne Simon-Gillo et al. "Deuteron and anti-deuteron production in CERN experiment NA44". In: *Nucl. Phys. A* 590 (1995). Ed. by Arthur M. Poskanzer, J. W. Harris, and L. S. Schroeder, pp. 483C–486C. DOI: 10.1016/0375-9474(95)00259-4.

[9] T. A. Armstrong et al. "Anti-deuteron yield at the AGS and coalescence implications". In: *Phys. Rev. Lett.* 85 (2000), pp. 2685–2688. DOI: 10.1103/PhysRevLett.85.2685. arXiv: nucl-ex/0005001.

[10] S. S. Adler et al. "Deuteron and antideuteron production in Au + Au collisions at $\sqrt{s_{\rm NN}}$ = 200 GeV". In: *Phys. Rev. Lett.* 94 (2005), p. 122302. DOI: 10.1103/PhysRevLett.94.122302. arXiv: nucl-ex/0406004.

[11] S. Henning et al. "Production of Deuterons and anti-Deuterons in Proton Proton Collisions at the CERN ISR". In: *Lett. Nuovo Cim.* 21 (1978), p. 189. DOI: 10.1007/BF02822248.

[12] A. Aktas et al. "Measurement of anti-deuteron photoproduction and a search for heavy stable charged particles at HERA". In: *Eur. Phys. J. C* 36 (2004), pp. 413–423. DOI: 10.1140/epjc/s2004-01978-x. arXiv: hep-ex/0403056.

[13] D. M. Asner et al. "Anti-deuteron production in Upsilon(nS) decays and the nearby continuum". In: *Phys. Rev. D* 75 (2007), p. 012009. DOI: 10.1103/PhysRevD.75.012009. arXiv: hep-ex/0612019.

[14] S. Schael et al. "Deuteron and anti-deuteron production in e^+ e^- collisions at the Z resonance". In: *Phys. Lett. B* 639 (2006), pp. 192–201. DOI: 10.1016/j.physletb.2006.06.043. arXiv: hep-ex/0604023.

[15] Shreyasi Acharya et al. "Multiplicity dependence of (anti-)deuteron production in pp collisions at $\sqrt{s}$ = 7 TeV". In: *Phys. Lett. B* 794 (2019), pp. 50–63. DOI: 10.1016/j.physletb.2019.05.028. arXiv: 1902.09290 [nucl-ex].

[16] H. Agakishiev et al. "Observation of the antimatter helium-4 nucleus". In: *Nature* 473 (2011). [Erratum: Nature 475, 412 (2011)], p. 353. DOI: 10.1038/nature10079. arXiv: 1103.3312 [nucl-ex].

[17] Francesca Bellini et al. "Examination of coalescence as the origin of nuclei in hadronic collisions". In: *Phys. Rev. C* 103.1 (2021), p. 014907. DOI: 10.1103/PhysRevC.103.014907. arXiv: 2007.01750 [nucl-th].

[18] M. Kachelriess, S. Ostapchenko, and J. Tjemsland. "On nuclear coalescence in small interacting systems". In: *Eur. Phys. J. A* 57.5 (2021), p. 167. DOI: 10.1140/epja/s10050-021-00469-w. arXiv: 2012.04352 [hep-ph].

[19] Jaroslav Adam et al. "Production of light nuclei and anti-nuclei in pp and Pb-Pb collisions at energies available at the CERN Large Hadron Collider". In: *Phys. Rev. C* 93.2 (2016), p. 024917. DOI: 10.1103/PhysRevC.93.024917. arXiv: 1506.08951 [nucl-ex].

[20] A. Andronic et al. "Production of light nuclei, hypernuclei and their antiparticles in relativistic nuclear collisions". In: *Phys. Lett. B* 697 (2011), pp. 203–207. DOI: 10.1016/j.physletb.2011.01.053. arXiv: 1010.2995 [nucl-th].

[21] J. Cleymans et al. "Antimatter production in proton-proton and heavy-ion collisions at ultrarelativistic energies". In: *Phys. Rev. C* 84 (2011), p. 054916. DOI: 10.1103/PhysRevC.84.054916. arXiv: 1105.3719 [hep-ph].

[22] S. T. Butler and C. A. Pearson. "Deuterons from High-Energy Proton Bombardment of Matter". In: *Phys. Rev.* 129 (1963), pp. 836–842. DOI: 10.1103/PhysRev.129.836.

[23] Rudiger Scheibl and Ulrich W. Heinz. "Coalescence and flow in ultrarelativistic heavy ion collisions". In: *Phys. Rev. C* 59 (1999), pp. 1585–1602. DOI: 10.1103/PhysRevC.59.1585. arXiv: nucl-th/9809092.

[24] Max Born. "Cosmic rays and the new field theory". In: *Nature* 133.3350 (1934), pp. 63.2–64. DOI: 10.1038/133063b0.

[25] A. W. Strong and I. V. Moskalenko. "Propagation of cosmic-ray nucleons in the galaxy". In: *Astrophys. J.* 509 (1998), pp. 212–228. DOI: 10.1086/306470. arXiv: astro-ph/9807150.

[26] Andrew W. Strong and Igor V. Moskalenko. "Modeling cosmic rays and gamma-rays in the galaxy". In: *AIP Conf. Proc.* 410.1 (1997), p. 1162. DOI: 10.1063/1.54096. arXiv: astro-ph/9709211.

[27] Luis Anchordoqui et al. "Ultrahigh-energy cosmic rays: The State of the art before the Auger Observatory". In: *Int. J. Mod. Phys. A* 18 (2003), pp. 2229–2366. DOI: 10.1142/S0217751X03013879. arXiv: hep-ph/0206072.

[28] Igor V. Moskalenko et al. "Secondary anti-protons and propagation of cosmic rays in the galaxy and heliosphere". In: *Astrophys. J.* 565 (2002), pp. 280–296. DOI: 10.1086/324402. arXiv: astro-ph/0106567.

[29] Alejandro Ibarra and Sebastian Wild. "Prospects of antideuteron detection from dark matter annihilations or decays at AMS-02 and GAPS". In: *JCAP* 02 (2013), p. 021. DOI: 10.1088/1475-7516/2013/02/021. arXiv: 1209.5539 [hep-ph].

[30] Marco Cirelli et al. "Anti-helium from Dark Matter annihilations". In: *JHEP* 08 (2014), p. 009. DOI: 10.1007/JHEP08(2014)009. arXiv: 1401.4017 [hep-ph].

[31] Michael Korsmeier, Fiorenza Donato, and Nicolao Fornengo. "Prospects to verify a possible dark matter hint in cosmic antiprotons with antideuterons and antihelium". In: *Phys. Rev. D* 97.10 (2018), p. 103011. DOI: 10.1103/PhysRevD.97.103011. arXiv: 1711.08465 [astro-ph.HE].

[32] N. Fornengo, L. Maccione, and A. Vittino. "Dark matter searches with cosmic antideuterons: status and perspectives". In: *JCAP* 09 (2013), p. 031. DOI: 10.1088/1475-7516/2013/09/031. arXiv: 1306.4171 [hep-ph].

[33] T. Aramaki et al. "Review of the theoretical and experimental status of dark matter identification with cosmic-ray antideuterons". In: *Phys. Rept.* 618 (2016), pp. 1–37. DOI: 10.1016/j.physrep.2016.01.002. arXiv: 1505.07785 [hep-ph].

[34] H. S. Ahn et al. "Measurements of cosmic-ray secondary nuclei at high energies with the first flight of the CREAM balloon-borne experiment". In: *Astropart. Phys.* 30 (2008), pp. 133–141. DOI: 10.1016/j.astropartphys.2008.07.010. arXiv: 0808.1718 [astro-ph].

[35] N. Saffold et al. "Cosmic antihelium-3 nuclei sensitivity of the GAPS experiment". In: *Astropart. Phys.* 130 (2021), p. 102580. DOI: 10.1016/j.astropartphys.2021.102580. arXiv: 2012.05834 [hep-ph].

[36] Roberto Battiston. "The antimatter spectrometer (AMS-02): A particle physics detector in space". In: *Nucl. Instrum. Meth. A* 588 (2008). Ed. by Antonio Capone et al., pp. 227–234. DOI: 10.1016/j.nima.2008.01.044.

[37] Shreyasi Acharya et al. "Measurement of the low-energy antideuteron inelastic cross section". In: *Phys. Rev. Lett.* 125.16 (2020), p. 162001. DOI: 10.1103/PhysRevLett.125.162001. arXiv: 2005.11122 [nucl-ex].

[38] E. Abbas et al. "Mid-rapidity anti-baryon to baryon ratios in pp collisions at $\sqrt{s} = 0.9$, 2.76 and 7 TeV measured by ALICE". In: *Eur. Phys. J. C* 73 (2013), p. 2496. DOI: 10.1140/epjc/s10052-013-2496-5. arXiv: 1305.1562 [nucl-ex].

[39] P.Larionov. *Measurement of (anti-)3He hadronic interaction cross-section in Pb-Pb collisions*. ALICE Analysis Note ALICE-ANA-1106. PWG-LF, 2021. URL: https://alice-notes.web.cern.ch/node/1106.

[40] Shreyasi Acharya et al. "The ALICE Transition Radiation Detector: construction, operation, and performance". In: *Nucl. Instrum. Meth. A* 881 (2018), pp. 88–127. DOI: 10.1016/j.nima.2017.09.028. arXiv: 1709.02743 [physics.ins-det].

[41] Betty Bezverkhny Abelev et al. "Performance of the ALICE Experiment at the CERN LHC". In: *Int. J. Mod. Phys. A* 29 (2014), p. 1430044. DOI: 10.1142/S0217751X14300440. arXiv: 1402.4476 [nucl-ex].

[42] K. Aamodt et al. "The ALICE experiment at the CERN LHC". In: *JINST* 3 (2008), S08002. DOI: 10.1088/1748-0221/3/08/S08002.

[43] K Aamodt et al. "Alignment of the ALICE Inner Tracking System with cosmic-ray tracks". In: *JINST* 5 (2010), P03003. DOI: 10.1088/1748-0221/5/03/P03003. arXiv: 1001.0502 [physics.ins-det].

[44] J. Alme et al. "The ALICE TPC, a large 3-dimensional tracking device with fast readout for ultra-high multiplicity events". In: *Nucl. Instrum. Meth. A* 622 (2010), pp. 316–367. DOI: 10.1016/j.nima.2010.04.042. arXiv: 1001.1950 [physics.ins-det].

[45] Stefan Roesler, Ralph Engel, and Johannes Ranft. "The Monte Carlo event generator DPMJET-III". In: *International Conference on Advanced Monte Carlo for Radiation Physics, Particle Transport Simulation and Applications (MC 2000)*. Dec. 2000, pp. 1033–1038. DOI: 10.1007/978-3-642-18211-2_166. arXiv: hep-ph/0012252.

[46] R. Brun et al. *GEANT3*. Tech. rep. CERN-DD-EE-84-1. 1987.

[47] J. Allison et al. "Recent developments in Geant4". In: *Nucl. Instrum. Meth. A* 835 (2016), pp. 186–225. DOI: 10.1016/j.nima.2016.06.125.

[48] D. Ashery et al. "True Absorption and Scattering of Pions on Nuclei". In: *Phys. Rev. C* 23 (1981), pp. 2173–2185. DOI: 10.1103/PhysRevC.23.2173.

[49] P. Schwaller et al. "Proton total cross-sections on H-1, H-2, He-4 Be-9, C and O in the energy range 180-MeV to 560-MeV". In: *Nucl. Phys. A* 316 (1979), pp. 317–344. DOI: 10.1016/0375-9474(79)90040-X.

[50] W. Bauhoff. "Tables of reaction and total cross sections for proton-nucleus scattering below 1 GeV". In: *Atom. Data Nucl. Data Tabl.* 35 (1986), pp. 429–447. DOI: 10.1016/0092-640X(86)90016-1.

[51] B. M. Bobchenko et al. "Measurement of total inelastic cross-sections from proton interactions with nuclei in the momentum range from 5-GeV/c to 9-GeV/c and pi- mesons with nuclei in the momentum range from 1.75 GeV/c to 6.5 GeV/c". In: *Sov. J. Nucl. Phys.* 30 (1979), p. 805.

[52] M. Tanabashi et al. "Review of Particle Physics". In: *Phys. Rev. D* 98.3 (2018), p. 030001. DOI: 10.1103/PhysRevD.98.030001.

[53] H. Fesefeldt. *The Simulation of Hadronic Showers: Physics and Applications*. Tech. rep. PITHA-85-02. 1985.

[54] P. A. Zyla et al. "Review of Particle Physics". In: *PTEP* 2020.8 (2020), p. 083C01. DOI: 10.1093/ptep/ptaa104.

[55] I.Vorobyev. *Constraining anti-deuteron inelastic interaction cross-section via anti-deuteron to deuteron ratio in p-Pb collisions at 5.02 TeV*. ALICE Analysis Note ALICE-ANA-887. PWG-LF, 2020. URL: https://alice-notes.web.cern.ch/node/887.

List of Tables

List of Figures

Acknowledgements

I want to thank Professor Laura Fabbietti for giving me the chance to work in this research group and for involving me in all the events and discussions throughout this year. In general I want to thank all members of the E62 department, who have been kind to me since day one and have always showed themselves willing to help. I want to do of course a spetial mention to my direct supervisor, Dr. Ivan Vorobyev, who has always been available and helping me for the completion of this project. Another spetial mention I would like to write for Dr. Luca Barioglio, with whom I had the chance to work the last weeks and who has taught me and helped me a lot in this short period of time.

On a personal note, I would like to thank everyone who has been a part of my life in this whole period of my master. It is fortunately impossible to name you all, but there are definitely some people I can not leave behind: Edipo, Anja, Alice, Sebastian, Mario, Pedro, I can not picture these years without you.

Finally, of course, I want to thank the people who have made this possible. To my aunt and my uncle, who helped me in a very stiff beginning and who have been by my side all the way. To my parents, whose support in all senses was key to make this happen. Even though we had to see each other much less than what we would have wanted, there was not a single day I did not feel you standing close to me. And last but not least at all, to you, Elisenda. This success is yours as much as it is mine. Thank you for your help and for your moral support.

Ohne euch wäre das alles nicht möglich gewesen.